Quiescent and Active Phases in Be Stars: A *WISE* Snapshot of Young Galactic Open Clusters

A. Granada[1,2], C. E. Jones[1] , T. A. A. Sigut[1] , T. Semaan[3], C. Georgy [3] , G. Meynet[3], and S. Ekström[3]
[1] Department of Physics and Astronomy, The University of Western Ontario, London, ON N6A 3K7, Canada; granada@fcaglp.unlp.edu.ar
[2] Now at Instituto de Astrofísica La Plata, CCT La Plata, CONICET-UNLP, Paseo del Bosque S/N, B1900FWA La Plata, Argentina
[3] Geneva Observatory, University of Geneva, Maillettes 51, CH-1290 Sauverny, Switzerland

Abstract

Through the modeling of near-infrared photometry of star-plus disk systems with the codes BEDISK/BERAY, we successfully describe the *Wide-Field Infrared Survey Explorer* (*WISE*) photometric characteristics of Be stars in five young open clusters, NGC 663, NGC 869, NGC 884, NGC 3766, and NGC 4755, broadly studied in the literature. *WISE* photometry allows previously known Be stars to be detected and to find new Be candidates which could be confirmed spectroscopically. The location of Be stars in the *WISE* color–magnitude diagram, separates them in two groups; active (Be stars hosting a developed circumstellar disk) and quiescent objects (Be stars in a diskless phase), and this way, we can explore how often stars are observed in these different stages. The variability observed in most active variable Be stars is compatible with a disk dissipation phase. We find that 50% of Be stars in the studied open clusters are in an active phase. We can interpret this as Be stars having a developed circumstellar disk one-half of the time. The location of Be stars with a developed disk in the color–magnitude diagram require mass loss rates in agreement with values recently reported in the literature. For these objects, we expect to have a tight relation between the equivalent width of the Hα line and the mass of the disk, if the inclination is known. Also, near-infrared photometry of Be stars in stellar clusters has the potential of being useful to test whether there is a preferential viewing angle.

Key words: infrared: stars – open clusters and associations: general – stars: activity – stars: emission-line, Be

1. Introduction

Be stars as a group are among the most rapidly rotating stars, both in terms of their spin angular velocity rate ($\Omega_{eq}/\Omega_{crit}$) and their equatorial velocity (V_{eq}). The defining observed characteristics of these main-sequence (MS), intermediate-mass stars include the presence of hydrogen and metallic lines in emission in their spectra, an infrared color excess, as well as short and long-term photometric and spectroscopic variability. These observed characteristics, together with radio observations, polarimetric signatures and interferometric data, can be globally explained within the framework of the viscous decretion disk model (for a recent review on this subject, we refer the reader to Rivinius et al. 2013). However, despite all the progress in understanding the characteristics of Be stars and their circumstellar disks, the underlying mechanism(s) triggering the formation of such a circumstellar envelope remains elusive.

According to Sana et al. (2012), over 70% of stars with masses larger than 8 $M_\odot$ exchange mass with a companion during some period of their evolution. Therefore a significant number of binaries is expected among B stars, in particular among earlier spectral types. For instance, the bimodal distribution of rotational velocities for the single early B-type stars found in the 30 Doradus region by Dufton et al. (2013), could be partly due to evolutionary effects related to binarity. An incidence of 30% of binarity among Be stars was found by Oudmaijer & Parr (2010), consistent with the incidence among normal, MS B stars. According to these authors, binarity may not be a key aspect involved in the appearance of the Be phenomenon; however, when the companion is close enough to the Be star, it could affect the circumstellar disk, for instance, by truncating it or triggering disk oscillations (e.g., Okazaki

et al. 2002; Oktariani et al. 2016). In other binary systems, episodes of mass transfer, or even mergers, could lead to the formation of a rapidly rotating star that could potentially become a Be star.

Understanding how the existence of Be stars depends on metallicity, spectral type, and evolutionary stage can help us to understand the mechanism(s) involved in the appearance of the Be phenomenon. Open clusters constitute ideal laboratories to study the conditions in which Be stars form and evolve. We can assume that cluster stars come from the same primordial cloud and share a common spatial location, proper motions, initial chemical composition, and age.

It has been long known that the detected fraction of Be stars with color excess increases with wavelength (e.g., Dougherty et al. 1994), as expected if the excess emission comes from free–free and bound-free processes occurring in their circumstellar disks. That is why the near-infrared (near-IR) spectral regions are particularly useful in detecting and confirming Be stars. IR surveys such as *Spitzer* (the fourth and final of the NASA Great Observatories program, an infrared space telescope launched in 2003) and AKARI (an infrared astronomy satellite developed by Japan Aerospace Exploration Agency, in cooperation with institutes of Europe and Korea, launched in 2006) have shown that the near-IR spectral region allows photometric detection and confirmation of Be stars (Bonanos et al. 2010; Ita et al. 2010).

The *Wide-Field Infrared Survey Explorer* (*WISE*, Wright et al. 2010), which surveyed the sky in four bandpasses between 3.4 μm and 22 μm, provides a better understanding of the infrared sky. The AllWISE source catalog (Cutri et al. 2013) gives observations with good angular resolution which are suitable to study the Be stellar population in open clusters.

Table 1
Selected Open Clusters

Name	Age[a] (log(year))	μ_0[a] (mag)	$E(B-V)$[a] (mag)	R_{cl}[a] (arcmin)
NGC 663	7.50	11.61	0.700	14.4
NGC 869	7.28	11.81	0.520	14.4[c]
NGC 884	7.20	11.85	0.560	10.5[c]
NGC 3766	7.40[b]	11.13	0.208	13.8
NGC 4755	7.30	11.47	0.396	13.5

Notes.
[a] Kharchenko et al. (2013) estimate errors for $E(B-V)$, age, distance, and radius of 7%, 39%, 11%, and 25%, respectively. The error estimate in distance of 11% corresponds to an error of the absolute distance modulus of 0.275 mag.
[b] This cluster age, which adequately describes the cluster turn-off and presence of red supergiant stars using SYCLIST, was not taken from Kharchenko et al. (2013).
[c] The cluster radii considered for these two clusters correspond to the angular radius of the central part (R1) by Kharchenko et al. (2013), instead of the angular radius of the cluster (R2). This is to avoid cluster overlapping.

In the present article, we use the IR photometry provided by the AllWISE source catalog (Cutri et al. 2013) for a group of five open clusters with ages between 10 and 30 Myr, well known for hosting Be stars and which have been extensively studied in the literature. We explore how these cluster Be stars are distributed in the *WISE* color–magnitude diagram (CMD) and investigate whether the location of Be stars in these plots can provide global information on the characteristics of the circumstellar disks and activity cycles for these stars. In order to interpret the observed near-IR characteristics of Be stars in open clusters, we generate a grid of synthetic *WISE* magnitudes and colors for star-plus-disk systems using the BERAY code (Sigut 2011).

This paper is organized as follows. In Section 2, we describe the observations and selection method. Section 3 presents our results, Section 4 describes our disk model predictions, and conclusions are provided in Section 5.

2. WISE Photometry of Young Open Clusters

2.1. WISE Observations

For the present work, we use data available at the AllWISE source catalog (Cutri et al. 2013). This program extended the work of the successful *WISE* survey (Wright et al. 2010), by combining data from different phases of the mission. AllWISE provides astrometry and photometry in four bandpasses in 3.4 μm (*W1*), 4.6 μm (*W2*), 12 μm (*W3*), and 22 μm (*W4*), for nearly 750 million objects, with a better sensitivity than the *WISE* All-Sky Release Catalog. Faint source flux biases were corrected, and a more robust estimation of the background level was obtained.

The angular resolution in *W1*, *W2*, *W3*, and *W4* bands are 6″.1, 6″.4, 6″.5, and 12″.0, respectively (Wright et al. 2010). As described in the AllWISE Data Processing documents, the AllWISE Source Catalog is intended to be a highly reliable and complete set of single, unique detections for compact objects on the sky, so targets in severely crowded regions are not considered in the AllWISE Source Catalog. That is why in the present study, even though we might miss some targets, we are not affected by severely crowded regions.

For the *W1* and *W2* filters, the saturation limits are $W1 = 8$ mag and $W2 = 7$ mag, and the limiting magnitudes, for which the background level becomes an issue in crowded cluster regions, occurs at $W1 = 14$ mag and $W2 = 13.5$ (Cutri et al. 2013). Therefore, it is important for our work to select clusters in which MS B stars have a brightness below the saturation limit and above the limiting magnitude. This way, we ensure that most of the cluster members have small errors in the *W1* and *W2* bands. It is worth stating that some targets located in rather crowded cluster regions, or with a nearby bright star, could suffer from a poor background determination, which may lead to an underestimation of the brightness and larger error bars.

Most stars with brightness between the saturation limit and background level in the *W1* and *W2* bands, have a brightness that is fainter than the background sky level in the *W4* band. That is why we focus only in the *W1* and *W2* data and, eventually, the *W3* data for those objects with good quality observations.

2.2. The Selected Sample of Open Clusters

As we are interested in studying the general behavior of Be stars, we selected five Galactic, young, open clusters broadly studied in the literature: NGC 663, NGC 3766, NGC 4755, and the double cluster NGC 869–NGC 884. Not only are they known for being particularly rich in Be stars, but also the B-type stars within these clusters have a brightness below the saturation limit and above the limiting magnitude as discussed in the previous section.

Even though various authors give different values for the cluster parameters (e.g., Phelps & Janes 1994; Pigulski et al. 2001; Fabregat & Capilla 2005 for NGC 663, Slesnick et al. 2002; Keller et al. 2001; Marco & Bernabeu 2001; Maciejewski & Niedzielski 2007 for NGC 869 and NGC 884, Aidelman et al. 2012; Piatti et al. 1998; McSwain & Gies 2005 for NGC 3766 or Aidelman et al. 2012; Balona & Koen 1994; Sanner et al. 2001 for NGC 4755), we chose to use those reported by Kharchenko et al. (2013), which provides a homogeneous database. For all the clusters under study, the parameters given by these authors agree with others in the literature. The names, ages, distance modulus, reddening, and radius assumed for the selected clusters are listed in Table 1.

To select the probable, early-type, cluster MS members, we used the cluster radius given by Kharchenko et al. (2013) and the 2MASS photometry provided together with the *WISE* photometry (Cutri et al. 2013). We converted the observed J magnitude and $(J-H)$ color to absolute values using the tabulated distances and $E(B-V)$ excesses of Table 1 and the empirical relations for the extinction A_J and excess $E(J-H)$ given by Yuan et al. (2013). The extinction coefficients given by these authors agree with the average values obtained by Davenport et al. (2014) as determined from 5×10^5 stars.

2.3. Synthetic Populations with SYCLIST

Even though a detailed cluster parameter determination is beyond the scope of the present article, we generated synthetic stellar populations with SYCLIST, the Geneva population synthesis code (Georgy et al. 2014), with the aim of determining the regions in the CMD where we expect to have MS and red supergiant stars for different cluster ages. We seek to check whether the parameters chosen from the literature are

NGC 663
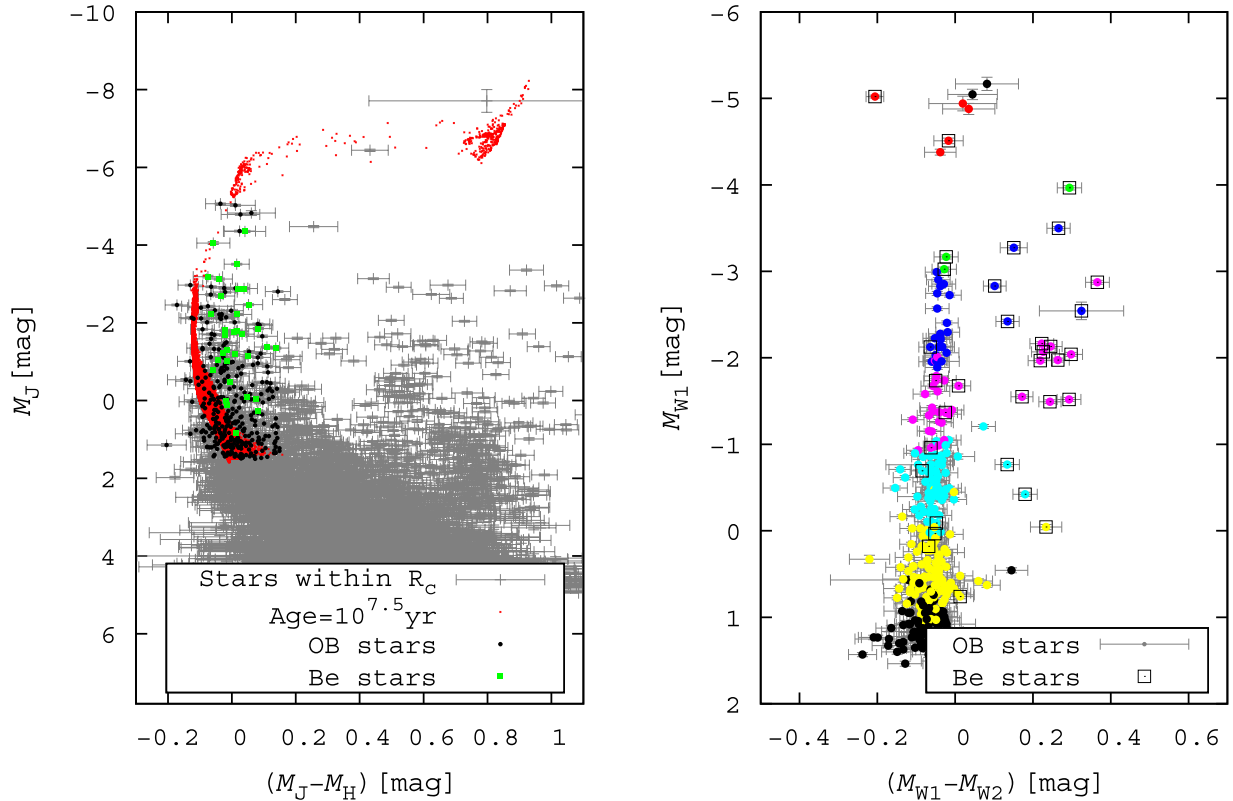
Figure 1. Color magnitude diagrams of the cluster NGC 663. Left: M_J vs. M_J-M_H plot. The gray symbols indicate all the objects within the cluster field. Black symbols correspond to cluster early-type MS stars and green small squares indicate known Be stars. Red points correspond to a synthetic stellar population computed with SYCLIST. Right: *WISE* M_{W1} vs. M_{W1}–M_{W2} for cluster members. Different colors correspond to different M_J magnitudes, a proxy of spectral type. Black open squares indicate known Be stars.

adequate to describe the observations. We decided to build stellar populations (as described in the next paragraph), instead of using typical isochrones, in order to account for the effects of stellar rotation in the evolution, as well as some observational effects.

Synthetic populations of 50,000 stars with masses between $1.7\,M_\odot$ and $15\,M_\odot$ at the ZAMS were created following the typical Salpeter initial mass function and the initial rotational velocity distribution given by Huang et al. (2010). The inclination angles (angle between the line of sight and the stellar rotation axis) are assumed to follow a random distribution. For these synthetic clusters, a fraction of 30% was adopted for unresolved binaries, which produces broadening in the low mass range where we have mainly equal mass binaries. We considered this value following Oudmaijer & Parr (2010), who found that the incidence of binaries among Be stars to be 30%. We used the color-effective temperature calibration from Worthey & Lee (2011). Because we do not intend to do detailed model fitting to the observations, we have not introduced artificial errors in magnitude and color to the stars in our synthetic clusters.

Figures 1–5 (left panels) show the synthetic populations (red dots) corresponding to the ages given by Kharchenko et al. (2013) together with the cluster observations, in the 2MASS M_J versus M_J–M_H CMD. All observed objects within the given cluster radius are indicated as gray crosses.

For NGC 3766, blue circles correspond to a synthetic population with a younger age than the one provided by Kharchenko et al. (2013), as has been proposed by different

authors for this cluster (Moitinho et al. 1997; Tadross 2001; Aidelman et al. 2012), and also appears in the WEBDA.[4] The younger age is in better agreement with the existence of RSG stars and the large number of Be stars found in this cluster (Granada et al. 2013).

The synthetic populations indicate that objects with $J \leqslant 1.5$ and intrinsic color $J - H < 0.15$, correspond to MS stars of spectral type earlier than A0, and to blue supergiant (BSG) stars. Then, from all the stars within the given cluster radius, we selected objects within these magnitude and color limits. By doing this, we removed foreground and background non-cluster members, pre-MS stars (see, e.g., Bonatto et al. 2006), as well as red giants and red supergiant (RSG) stars. These objects are plotted as black points in Figures 1 to 5 (left panel).

For all the clusters, the region in the CMD occupied by MS stars, indicated with black points, is correctly traced by the models of ages given in Table 1, including the position of the cluster turn-off and the location of RSG stars.

2.4. The Selection of WISE B-type Stars

As mentioned in the previous subsection, the left panels of Figures 1–5 show the 2MASS CMD of absolute magnitude M_J versus the intrinsic color $J - H$ for synthetic clusters and observations.

---

[4] http://www.univie.ac.at/webda/webda.html

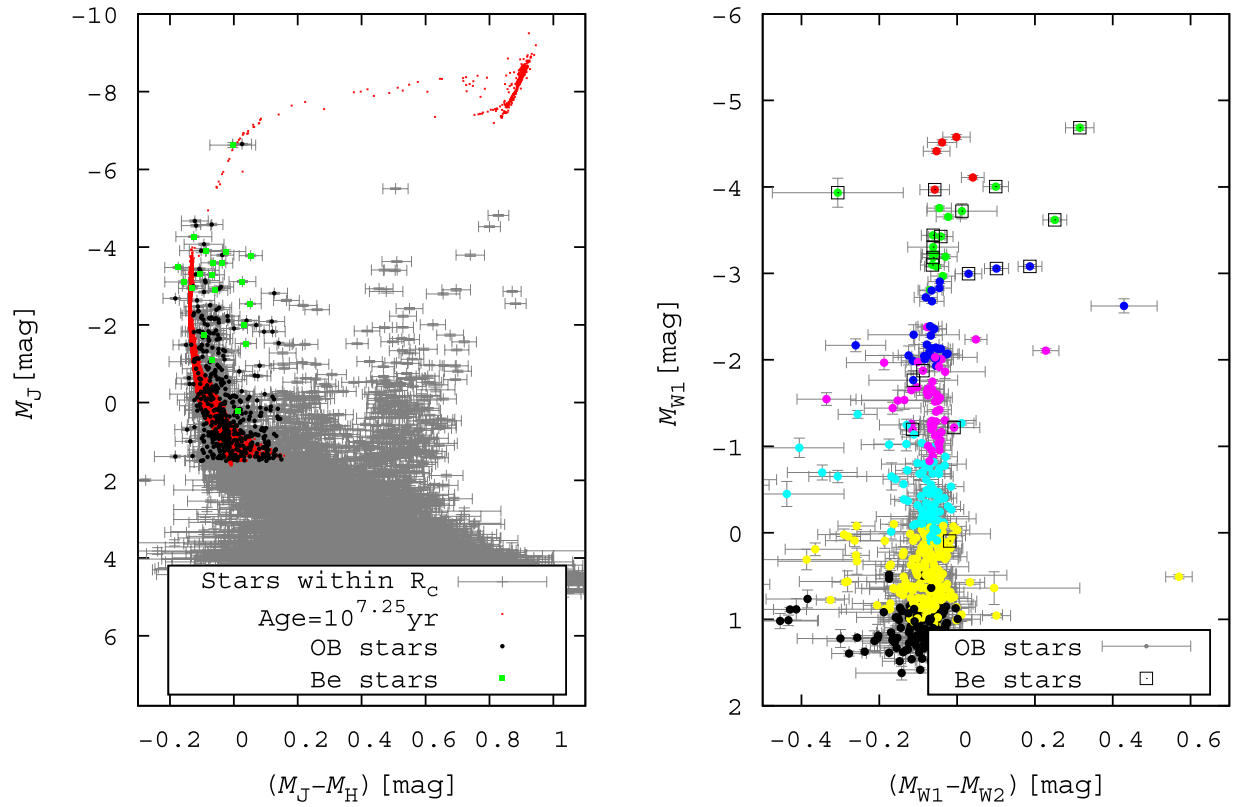**Figure 2.** The same as Figure 1 for the cluster NGC 869.

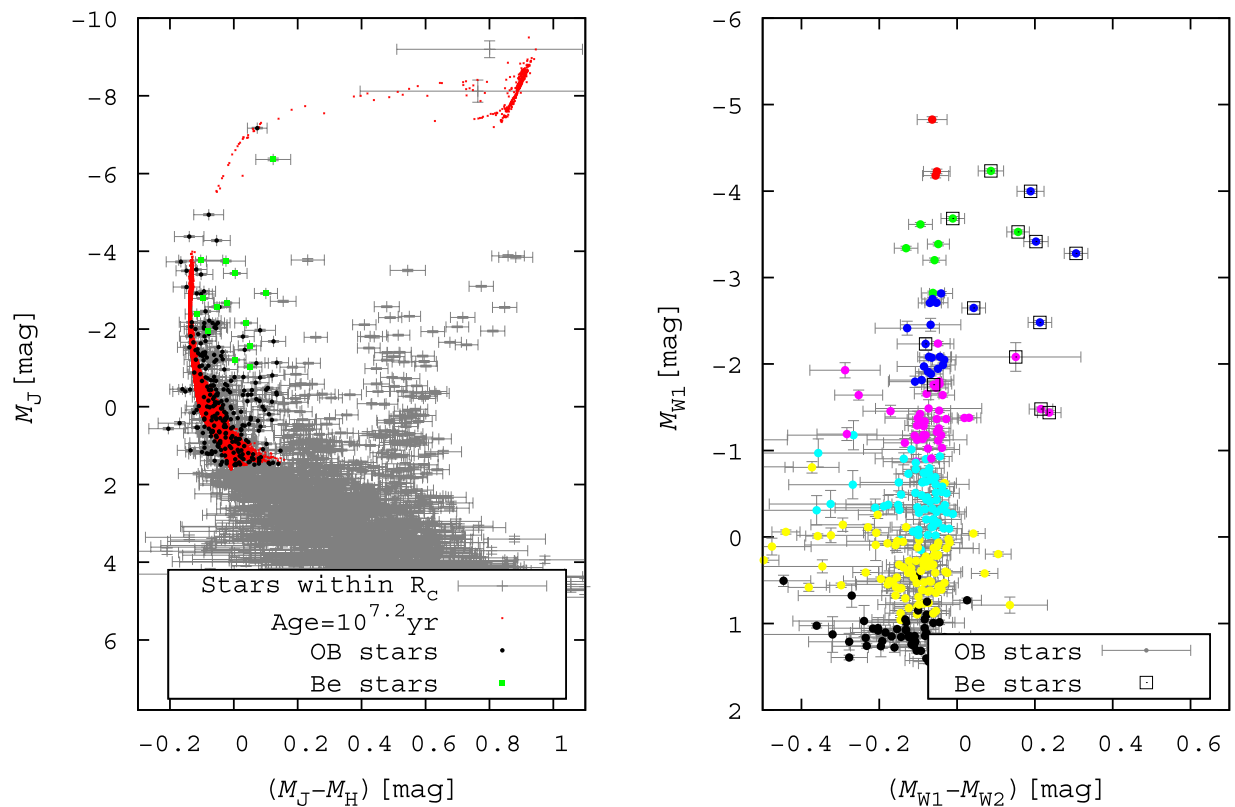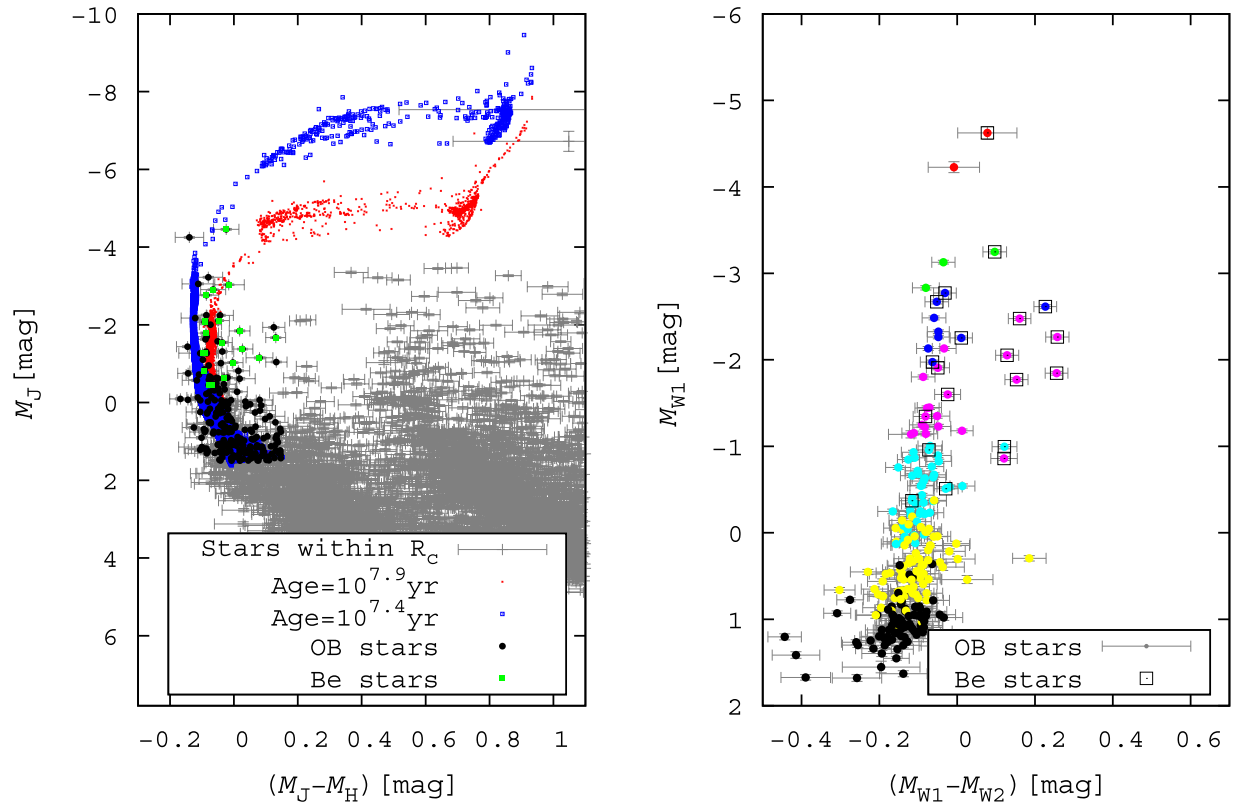**Figure 3.** The same as Figure 1 for the cluster NGC 884.

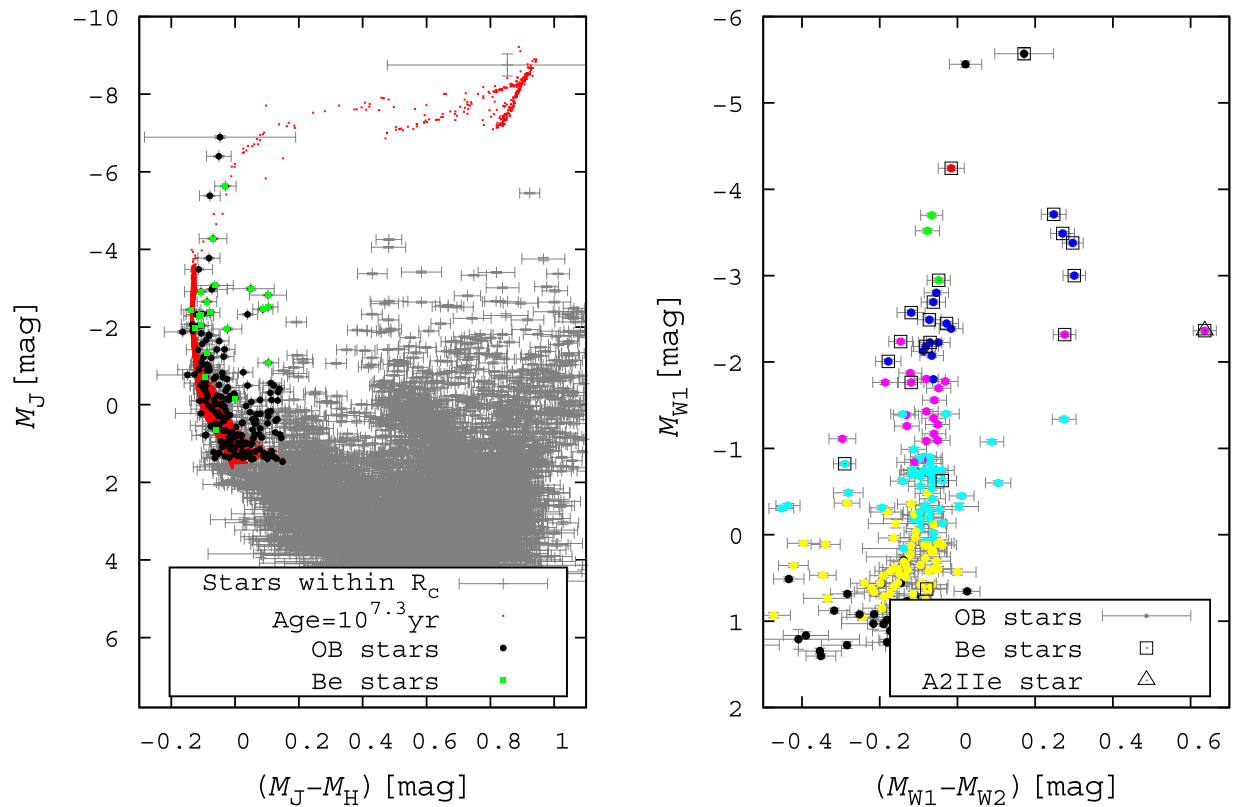**Figure 4.** The same as Figure 1 for the cluster NGC 3766.

**Figure 5.** The same as Figure 1 for the cluster NGC 4755.

5

Table 2
95 Be Stars Analyzed in This Work

R.A.	Decl.	M_{W1}	e M_{W1}	M_{W12}	e M_{W12}	M_{W23}	e M_{W23}	M_J	e M_J	M_H	e M_H	M_K	e M_K	Var	ST	LC	SIMBAD Name and Remarks	Be Class
(°)	(°)	(mag)	(mag)	(mag)	(mag)	(mag)	(mag)	(mag)	(mag)	(mag)	(mag)	(mag)	(mag)					
26.525441	61.227595	−2.55	0.10	0.32	0.11	1.21	0.05	−2.47	0.03	−2.52	0.04	−2.78	0.02	0	0.5	5	EM* VES 616, [1]	early
26.558441	61.228838	−0.77	0.02	0.13	0.03	0.50	⋯	−0.48	0.02	−0.48	0.03	−0.66	0.02	2	5	5	V* V979 Cas, [1]	late
26.508573	61.250567	−0.05	0.03	0.23	0.04	1.52	0.10	0.28	0.04	0.19	0.03	0.05	0.03	0	5	5	NGC 663 84, [1] *	late
26.584334	61.239349	−1.56	0.02	0.17	0.03	1.07	0.06	−1.71	0.02	−1.74	0.03	−1.90	0.02	0	2	5	EM* GGA 98, [1]	mid
26.497126	61.212676	−3.28	0.03	0.15	0.04	0.64	0.04	−2.69	0.03	−2.65	0.03	−2.66	0.02	0	0.5	5	BD+60 332A, [1]	early
26.483769	61.212565	−2.17	0.02	0.22	0.03	0.86	0.04	−1.85	0.02	−1.94	0.03	−2.15	0.02	3	2	5	EM* GGA 97, [1]	mid
26.612098	61.236493	−1.38	0.02	−0.03	0.03	0.48	0.07	−1.23	0.03	−1.21	0.04	−1.20	0.02	1	⋯	−	EM* GGA 99, [2] *	mid †
26.619315	61.230679	−0.70	0.02	−0.09	0.03	0.25	0.15	−0.78	0.02	−0.72	0.03	−0.81	0.02	1	3	5	NGC 663 14, [1]	late
26.627616	61.241449	−2.08	0.02	0.22	0.03	0.78	0.04	−1.29	0.02	−1.27	0.03	−1.36	0.02	1	1	5	V* V984 Cas, [1]	mid
26.615266	61.207074	−2.84	0.02	0.10	0.03	0.75	0.04	−2.86	0.02	−2.88	0.03	−2.92	0.02	1	5	⋯	V* V983 Cas, [3] *	early
26.648359	61.227523	−1.98	0.02	0.26	0.03	1.01	0.04	−1.35	0.03	−1.49	0.03	−1.70	0.02	0	1	5	EM* GGA 101, [1]	mid
26.449515	61.273316	−0.10	0.02	−0.05	0.03	0.60	0.14	−0.05	0.02	−0.13	0.03	−0.08	0.02	1	⋯	−	2MASSJ01454789 + 6116239, [2]	late †
26.415063	61.216452	−1.50	0.02	0.24	0.03	1.09	0.04	−1.19	0.02	−1.20	0.03	−1.33	0.02	0	2	5	EM* GGA 94, [1]	mid
26.601678	61.177033	0.17	0.03	−0.07	0.03	1.42	0.14	0.11	0.02	0.13	0.04	0.10	0.02	1	6	5	NGC 663 61, [1]	late
26.672702	61.220864	−2.13	0.02	−0.07	0.03	0.10	0.07	−2.22	0.03	−2.15	0.03	−2.12	0.02	0	4	⋯	EM* GGA 622, [2]	early
26.612723	61.167195	−3.03	0.02	−0.03	0.03	−0.04	0.07	−3.13	0.03	−3.09	0.03	−3.00	0.02	1	5	3	BD+60 340, [3]	early
26.689256	61.199832	−0.97	0.02	−0.07	0.03	−1.15	⋯	−1.05	0.03	−1.01	0.03	−0.93	0.02	1	⋯	−	EM* VES 623, [4]	mid †
26.443298	61.155813	−2.14	0.02	0.24	0.03	0.87	0.03	−1.79	0.02	−1.81	0.03	−1.93	0.02	0	1	5	EM* GGA 95, [1]	mid
26.641521	61.150654	−3.17	0.02	−0.03	0.03	0.32	0.05	−3.19	0.04	−3.11	0.03	−3.09	0.02	1	2	5	BD+60 334, [2]	early
26.748328	61.208206	−0.43	0.02	0.18	0.03	1.41	0.09	−0.08	0.02	−0.13	0.03	−0.23	0.02	1	5	5	EM* VES 624, [1]	late
26.611840	61.128259	−3.51	0.02	0.26	0.03	0.85	0.03	−2.89	0.02	−2.92	0.04	−3.15	0.02	1	0.5	5	BD+60 341, [1]	early
26.407547	61.133112	−1.98	0.02	0.22	0.03	0.75	0.05	−1.01	0.03	−1.00	0.04	−1.18	0.02	1	2	5	EM* GGA 93, [1] *	mid
26.765592	61.292237	−1.53	0.02	0.29	0.03	1.13	0.04	−1.14	0.02	−1.19	0.03	−1.29	0.02	3	2	5	V* V986 Cas, [1]	mid
26.634543	61.119229	−1.74	0.02	−0.05	0.03	0.29	0.07	−1.81	0.03	−1.78	0.03	−1.73	0.02	1	2	5	Cl* NGC 663 L604 [2]	mid
26.645246	61.107708	0.03	0.02	−0.06	0.03	1.99	0.10	0.01	0.03	0.03	0.04	0.07	0.02	1	5	5	NGC 663 180, [1]	late
26.822992	61.221549	0.75	0.03	0.01	0.04	0.27	⋯	0.85	0.03	0.84	0.03	0.80	0.03	1	6	5	NGC 663 151, [1]	late
26.325104	61.115690	−3.97	0.03	0.29	0.03	0.79	0.02	−3.51	0.03	−3.53	0.03	−3.63	0.02	0	1	5	BD+60 325, [1]	early
26.750870	61.356541	−2.43	0.02	0.13	0.03	0.63	0.03	−2.22	0.03	−2.23	0.04	−2.34	0.02	1	1	3	EM* GGA 104, [2]	early
26.861504	61.145601	−2.88	0.02	0.36	0.03	0.99	0.04	−1.69	0.03	−1.66	0.03	−1.59	0.02	2	0.5	5	EM* GGA 108, [1]	mid
26.914048	61.305712	−2.05	0.02	0.30	0.03	0.96	0.04	−1.38	0.03	−1.49	0.03	−1.68	0.02	1	1	5	EM* GGA 109, [1]	mid
26.739843	61.027863	−1.68	0.02	0.01	0.03	0.13	0.06	−1.76	0.02	−1.76	0.03	−1.89	0.02	3	3	⋯	EM* GGA 103 [2]	mid
34.737496	57.128716	−1.20	0.02	−0.12	0.03	−0.20	0.14	−1.08	0.05	−1.02	0.05	−1.06	0.04	1	3	⋯	[KPK99]J021856.82 + 570742.5, [5] *	mid
34.740807	57.138137	−1.88	0.02	−0.09	0.03	−0.18	0.09	−1.75	0.03	−1.65	0.03	−1.60	0.02	1	2	4	NSV 776 [6]	mid
34.750714	57.145720	−3.00	0.02	0.03	0.03	0.25	0.04	−2.94	0.02	−2.81	0.04	−2.79	0.02	1	1	5	V* V614 Per, [5]	early
34.724407	57.139512	−3.19	0.02	−0.06	0.03	0.01	0.04	−3.30	0.03	−3.20	0.03	−3.16	0.02	1	0.5	5	BD+56 515, [1]	early
34.806949	57.128771	−3.63	0.02	0.25	0.03	0.71	0.03	−3.12	0.03	−3.14	0.03	−3.29	0.02	1	1	5	BD+56 529, [1]	early
34.864416	57.138239	−3.45	0.02	−0.06	0.03	0.06	0.03	−3.60	0.03	−3.53	0.03	−3.43	0.02	1	0.5	5	HD 14162, [5]	early
34.870057	57.117908	−3.09	0.02	0.19	0.03	0.44	0.03	−2.54	0.02	−2.60	0.03	−2.76	0.02	2	0.5	5	EM* GGA 156, [1]	early
34.699721	57.067204	−4.01	0.03	0.10	0.03	0.57	0.03	−3.89	0.04	−3.86	0.05	−3.87	0.02	1	0.5	5	BD+56 511, [1]	early
34.815054	57.188465	0.09	0.02	−0.02	0.03	0.01	⋯	0.23	0.03	0.21	0.03	0.19	0.02	1	10	⋯	2MASSJ02191561 + 5711185, [5]	late
34.624291	57.150883	−3.10	0.02	−0.07	0.03	0.05	0.04	−3.29	0.02	−3.22	0.03	−3.15	0.02	1	0.5	1	V* V611 Per, $T_{eff} = 25400$K, $\log g = 3.38$, [7]	early
34.860474	57.078364	−4.69	0.03	0.31	0.04	0.99	0.03	−3.78	0.03	−3.83	0.02	−4.10	0.02	1	3	5	BD+56 534, $T_{eff} = 26400$K, $\log g = 3.55$, [1]	early
34.870366	57.190083	−1.22	0.06	−0.01	0.07	0.33	0.08	−1.52	0.02	−1.56	0.03	−1.68	0.02	3	0.5	5	NGC 869 1278, $T_{eff} = 25100$K, $\log g = 4.24$, [1]	mid
34.636556	57.211031	−3.31	0.06	−0.06	0.07	0.04	0.03	−3.48	0.03	−3.30	0.03	−3.32	0.02	1	1	5	BD+56 502, $T_{eff} = 26700$K, $\log g = 3.91$, [7]	early
34.949225	57.111018	−1.77	0.11	−0.12	0.11	0.65	0.05	−2.00	0.02	−2.03	0.03	−2.10	0.02	2	2	⋯	2MASSJ02194783 + 5706395, $T_{eff} = 20709$K, $\log g = 3.94$, [6]	early
34.562878	57.171130	−3.06	0.02	0.10	0.03	0.60	0.03	−2.89	0.03	−2.83	0.03	−2.89	0.02	1	3	5	BD+56 489, [5]	early
34.700842	57.240094	−3.73	0.09	0.01	0.09	0.30	0.03	−3.10	0.03	−2.95	0.05	−2.91	0.04	3	1	⋯	NAME BD+56 509AB, [5] *	early
34.700054	57.285527	−3.43	0.02	−0.04	0.03	0.00	0.03	−3.59	0.02	−3.55	0.03	−3.43	0.02	1	2	5	V* V665 Per, [5]	early
35.573678	57.123500	−3.69	0.02	−0.01	0.03	0.55	0.03	−3.77	0.02	−3.67	0.07	−3.69	0.02	1	2	3	V* V622 Per, [8]	early
35.510306	57.155664	−2.49	0.02	0.21	0.03	0.67	0.04	−2.16	0.02	−2.20	0.03	−2.35	0.02	3	1	5	NGC 869 2242, [1]	early
35.709491	57.147412	−1.49	0.02	0.21	0.03	0.92	0.04	−1.21	0.02	−1.21	0.03	−1.26	0.02	3	3	⋯	2MASSJ02225028 + 5708506, [5]	mid
35.519004	57.177461	−2.24	0.07	−0.08	0.07	0.05	0.06	−2.39	0.02	−2.27	0.03	−2.25	0.02	1	2	5	EM* MWC 39, [1]	early
35.481492	57.099632	−1.77	0.02	−0.06	0.03	−0.17	0.09	−1.94	0.02	−1.86	0.03	−1.77	0.02	1	3	5	[CHI2010] h Per M2623, [5]	mid
35.470567	57.166364	−4.00	0.03	0.19	0.04	0.51	0.04	−2.79	0.02	−2.69	0.03	−2.61	0.02	1	1	5	BD+56 566, $T_{eff} = 24800$K, $\log g = 3.79$, [1]	early
35.430794	57.125830	−3.53	0.02	0.16	0.03	1.18	0.03	−3.43	0.02	−3.44	0.03	−3.44	0.02	3	1	3	BD+56 563, $T_{eff} = 21900$, $\log g = 3.72$, [7]	early
35.767418	57.127469	−2.65	0.02	0.04	0.03	0.66	0.03	−2.57	0.02	−2.52	0.03	−2.53	0.02	3	2	⋯	EM* GGA 163, [5]	early

Table 2
(Continued)

R.A.	Decl.	M_{W1}	e M_{W1}	M_{W12}	e M_{W12}	M_{W23}	e M_{W23}	M_J	e M_J	M_H	e M_H	M_K	e M_K	Var	ST	LC	SIMBAD Name and Remarks	Be Class
35.700408	57.200277	−3.28	0.02	0.30	0.03	0.93	0.03	−2.67	0.02	−2.65	0.03	−2.72	0.03	2	0.5	5	EM* MWC 711, [1], *	early
35.435269	57.181195	−2.09	0.17	0.15	0.17	0.89	0.04	−1.57	0.02	−1.62	0.03	−1.72	0.02	1	3	5	EM* GGA 162, [1]	mid
35.353822	57.197898	−1.44	0.02	0.24	0.03	0.94	0.04	−1.03	0.02	−1.08	0.03	−1.21	0.02	1	2	⋯	EM* GGA 161, [9]	mid
35.594727	57.284735	−4.24	0.03	0.09	0.03	0.62	0.03	−3.75	0.03	−3.73	0.06	−3.69	0.02	1	1	3	BD+56 582, [9]	early
35.887723	57.075727	−3.42	0.02	0.20	0.03	0.56	0.03	−2.92	0.02	−3.02	0.03	−3.21	0.02	3	⋯	⋯	TYC 3694-1331-1, $T_{\rm eff}$ = 22535K, log g = 3.94, [10]	early
174.090981	−61.608303	−0.96	0.02	−0.07	0.03	−0.72	0.44	−0.81	0.03	−0.72	0.03	−0.70	0.03	1	⋯	⋯	CPD-60 3149, $T_{\rm eff}$ = 16890K, log g = 3.84, [9]	late
174.091240	−61.624731	−1.00	0.02	0.12	0.03	0.60	0.07	−0.64	0.03	−0.61	0.03	−0.70	0.02	1	⋯	⋯	CPD-60 3144, $T_{\rm eff}$ = 17687K, log g = 3.61, [9]	late
174.058513	−61.626579	−1.35	0.02	−0.08	0.03	−0.02	0.08	−1.55	0.02	−1.51	0.02	−1.52	0.02	1	2	5	CPD-60 3133, $T_{\rm eff}$ = 17519K, log g = 3.69, [9]	mid
174.042312	−61.627764	−2.62	0.02	0.23	0.03	0.81	0.03	−2.11	0.02	−2.06	0.02	−2.05	0.02	3	1.5	5	CPD-60 3126, $T_{\rm eff}$ = 18564K, log g = 3.53 , [9]	early
174.049414	−61.597301	−2.78	0.02	−0.03	0.03	0.19	0.05	−2.91	0.02	−2.84	0.03	−2.77	0.02	1	2	5	CPD-60 3128, $T_{\rm eff}$ = 18817K, log g = 3.31, [9]	mid
174.039818	−61.593906	−2.26	0.02	0.01	0.03	0.34	0.04	−2.07	0.02	−1.98	0.02	−1.96	0.02	3	⋯	⋯	CPD-60 3125, $T_{\rm eff}$ = 18274K, log g = 3.49, [9]	early
174.088804	−61.587768	−1.91	0.02	−0.05	0.03	−0.31	0.12	−1.79	0.03	−1.70	0.03	−1.75	0.02	1	2	5	CPD-60 3147, $T_{\rm eff}$ = 18883K, log g = 3.23, [9]	mid
174.004467	−61.621609	−1.77	0.02	0.15	0.03	1.07	0.03	−1.28	0.02	−1.19	0.03	−1.15	0.03	3	⋯	⋯	CPD-60 3108, $T_{\rm eff}$ = 17792K, log g = 3.75, [9]	mid
174.033412	−61.643960	−2.27	0.02	0.26	0.03	0.80	0.03	−1.67	0.02	−1.80	0.02	−1.99	0.02	1	⋯	⋯	CPD-60 3122, $T_{\rm eff}$ = 13254K, log g = 3.29, [9]	mid
173.981095	−61.603857	−2.67	0.02	−0.05	0.03	0.08	0.06	−2.76	0.02	−2.68	0.03	−2.67	0.02	1	2	4	HD 100856, $T_{\rm eff}$ = 18725, log g = 3.34, [9]	early
174.131523	−61.573839	−3.25	0.02	0.10	0.03	0.42	0.03	−3.03	0.02	−3.02	0.04	−3.11	0.02	3	⋯	⋯	HD 306791, $T_{\rm eff}$ = 18399K, log g = 3.30, [9]	early
174.174609	−61.631627	−0.37	0.02	−0.12	0.03	−0.33	0.29	−0.46	0.03	−0.38	0.03	−0.38	0.03	1	⋯	⋯	CPD-60 3165, $T_{\rm eff}$ = 15945K, log g = 3.95, [9]	late
174.205566	−61.605880	−0.51	0.02	−0.03	0.03	0.09	0.08	−0.45	0.03	−0.38	0.02	−0.35	0.02	3	⋯	⋯	CPD-60 3174, $T_{\rm eff}$ = 15650, log g = 3.78, [9]	late
174.051578	−61.545558	−2.48	0.02	0.16	0.03	0.54	0.03	−1.27	0.03	−1.17	0.07	−1.15	0.05	1	⋯	⋯	CD-60 3626, $T_{\rm eff}$ = 17834K, log g = 3.82, [9]	mid
174.022890	−61.701685	−2.06	0.02	0.13	0.03	0.53	0.03	−1.85	0.02	−1.86	0.02	−2.00	0.02	1	⋯	⋯	HD 306797, $T_{\rm eff}$ = 16301K, log g = 3.51, [9]	mid
173.842030	−61.536173	−0.86	0.02	0.12	0.03	0.90	0.23	−1.03	0.02	−1.03	0.02	−1.08	0.02	3	⋯	⋯	HD 306793, $T_{\rm eff}$ = 18995K, log g = 4.02, [9]	mid
173.813207	−61.699876	−1.85	0.02	0.25	0.03	0.94	0.04	−1.38	0.02	−1.41	0.03	−1.57	0.02	3	⋯	⋯	HD 306657, $T_{\rm eff}$ = 19580K, log g = 4.00, [9]	mid
174.453112	−61.751439	−1.60	0.03	−0.03	0.03	−0.50	0.11	−1.15	0.03	−1.23	0.03	−1.39	0.02	1	⋯	⋯	CPD-60 3087, [11]	mid
193.432798	−60.374656	−2.45	0.02	−0.03	0.03	1.77	0.03	−2.29	0.03	−2.18	0.04	−2.18	0.02	2	1.5	5	V* CT Cru, [9]	early
193.446492	−60.372198	−3.71	0.02	0.25	0.03	0.97	0.03	−2.99	0.04	−3.04	0.06	−3.22	0.03	1	1.5	5	2MASS J12534725-6022200, $T_{\rm eff}$ = 25040K, log g = 3.91, [9]	early
193.465538	−60.366237	−2.01	0.03	−0.18	0.03	2.34	0.04	−2.04	0.02	−1.94	0.03	−1.83	0.02	2	1	5	V* CX Cru, [12]	early
193.356909	−60.366710	−1.77	0.02	−0.12	0.03	−0.45	0.08	−1.97	0.02	−1.84	0.02	−1.82	0.02	1	1	5	CPD-59 4532, [12]	mid
193.466655	−60.371088	−2.58	0.03	−0.12	0.04	0.40	0.05	−2.66	0.02	−2.57	0.02	−2.53	0.02	1	2	⋯	V* EI Cru, [12]	early
193.470570	−60.358505	−2.24	0.02	−0.15	0.03	0.60	0.04	−1.95	0.03	−1.93	0.04	−1.94	0.02	1	2	5	V* CZ Cru, [12]	mid
193.467558	−60.374383	−2.49	0.02	−0.07	0.03	0.47	0.03	−2.45	0.02	−2.31	0.02	−2.30	0.02	2	1.5	5	V* CY Cru, [12]	early
193.412417	−60.395461	−3.49	0.02	0.27	0.03	0.82	0.03	−2.82	0.02	−2.93	0.06	−3.16	0.02	1	2	4	CPD-59 4546, [13]	early
193.397882	−60.396305	−2.19	0.02	−0.08	0.03	−0.01	0.04	−2.38	0.02	−2.30	0.02	−2.20	0.02	1	1.5	5	V* BT Cru, [12]	early
193.464869	−60.388024	−3.38	0.02	0.30	0.03	0.73	0.03	−2.51	0.02	−2.62	0.02	−2.83	0.02	1	2	4	CPD-59 4559, [12]	early
193.469057	−60.399304	−0.63	0.03	−0.04	0.04	−0.59	0.25	−0.15	0.02	−0.15	0.03	−0.18	0.02	1	⋯	⋯	CPD-59 4561, [9]	late
193.445743	−60.309989	−2.23	0.02	−0.07	0.03	0.15	0.04	−2.31	0.02	−2.21	0.02	−2.18	0.02	1	1.5	5	V* CV Cru, [12]	early
193.489734	−60.416141	−2.70	0.02	−0.06	0.03	−0.01	0.05	−2.91	0.02	−2.81	0.05	−2.73	0.02	1	1	5	V* BW Cru, [12]	early
193.220361	−60.296769	0.63	0.03	−0.08	0.04	−0.18	⋯	0.65	0.02	0.71	0.03	0.71	0.03	1	⋯	⋯	Cl* NGC 4755 ESL 101, [14]	late
193.159809	−60.338676	−2.32	0.02	0.27	0.03	0.87	0.03	−1.33	0.02	−1.24	0.02	−1.20	0.02	1	⋯	⋯	HD 312076, [15]	mid †
193.150957	−60.307060	−3.00	0.02	0.30	0.03	0.90	0.03	−2.46	0.02	−2.55	0.02	−2.75	0.02	1	0	⋯	HD 312075, [15]	early

Note. (1) Mathew & Subramaniam (2011), (2) Pigulski et al. (2001), (3) Kohoutek & Wehmeyer (1997), (4) Coyne et al. (1978), (5) Abad & Garcia (1995), (6) Slesnick et al. (2002), (7) Marsh Boyer et al. (2012), (8) Høg et al. (2000), (9) McSwain et al. (2009), (10) Huang et al. (2010), (11) Slettebak (1985), (12) Sanner et al. (2001), (13) Jaschek & Egret (1982), (14) McSwain & Gies (2005), (15) Wray (1966). The symbol * in column 18 indicates that there is a source within 8asec of the target, for most of them significantly weaker. The symbol † in column 19 indicates that this is the first time an estimate of the spectral type is given for the star.
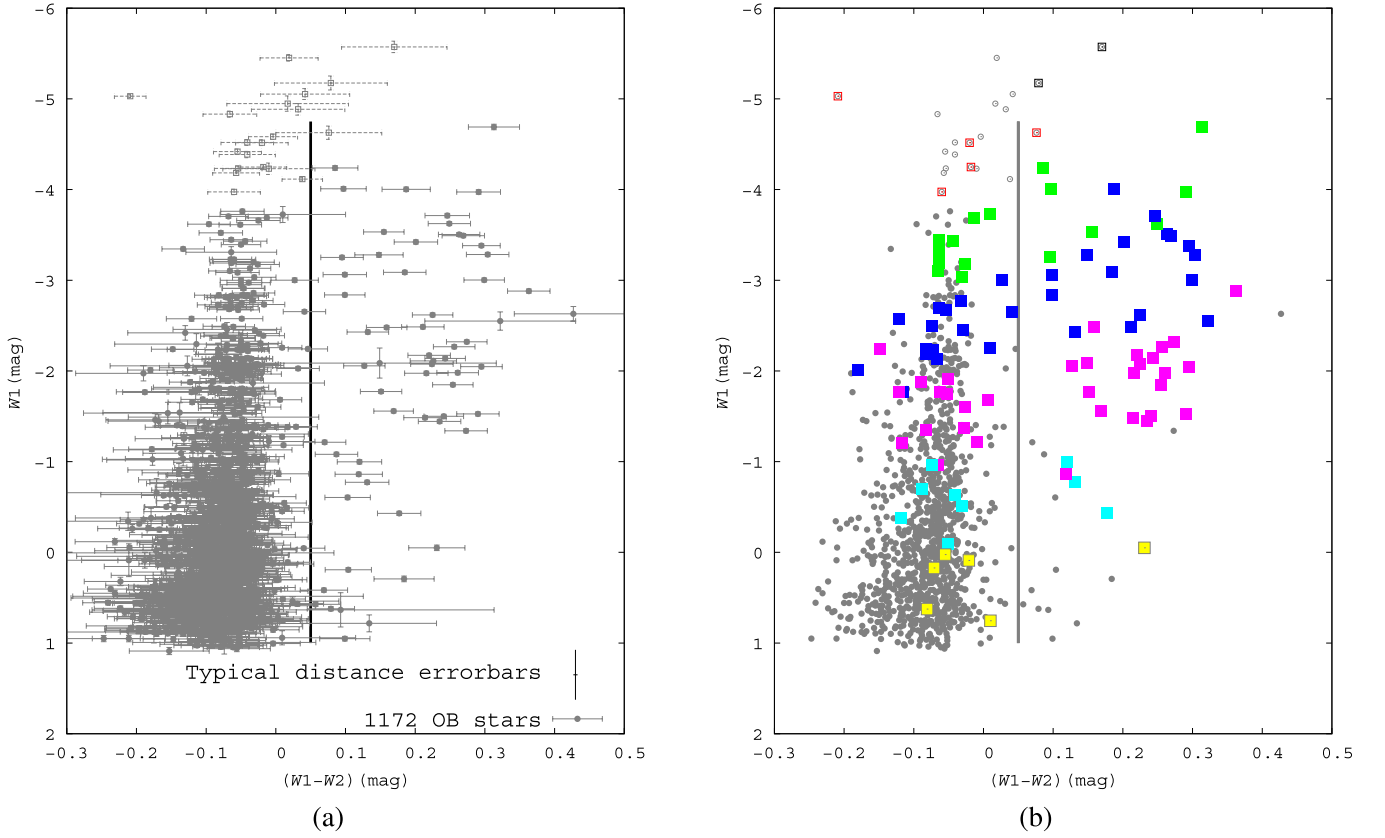
Figure 6. Color magnitude diagram of the 5 clusters. (a) All data points are shown with error bars and the vertical line indicates the color limit for *naked* stars ; (b) All known Be stars are indicated with colored squares with the different colors representing different absolute *J* magnitudes, an indication of spectral type.

Table 3
Be Candidates and Other Interesting Objects that Deserve Further Study

Cluster	R.A.	δ	M_{W1}	W12	W23	Simbad Name/Relevant Data
				Candidate Be		
NGC 663	01 45 55.876	+61 12 33.69	0.573	0.057	⋯	MV 34016[1]
	01 45 45.559	+61 10 55.47	−1.214	0.070	⋯	G 111[2]
	01 47 28.119	+61 22 45.95	0.622	0.079	⋯	⋯
NGC 869/884	02 18 34.121	+57 13 50.24	−2.630	0.427	⋯	HG 731[3], $V_{\text{proj}} = 165\,\text{km s}^{-1}$[4], $T_{\text{eff}} = 20561\text{K}$[4], log g = 3.944[4], SB1[3].
	02 19 03.292	+57 08 20.34	−2.111	0.226	0.492	W2[4], B2V, $T_{\text{eff}} = 20566\text{K}$[5], log g = 3.96[5], $V_{\text{proj}} = 171\,\text{km s}^{-1}$[5].
	02 19 51.091	+57 17 34.14	0.634	0.093	⋯	NGC 869 1455
	02 20 24.749	+57 06 53.07	0.952	0.099	⋯	LAV 1432[6]
	02 21 33.416	+57 12 01.62	0.783	0.134	⋯	LAV 1757[6]
	02 21 44.694	+57 04 09.23	0.192	0.104	⋯	LAV 1825[6]
	02 23 17.891	+57 14 23.71	0.417	0.069	⋯	LAV 2353[6]
NGC 3766	11 36 30.153	−61 39 47.62	0.293	0.184	1.130	MG 173[7], $V_{\text{proj}} = 171\,\text{km s}^{-1}$[8], $T_{\text{eff}} = 14210\text{K}$[8], log g = 4.21[8], He weak.
NGC 4755	12 53 37.775	−60 17 45.24	−1.340	0.273	2.331	SB 133[10]
	12 53 29.469	−60 21 16.56	−0.605	0.103	1.562	ESL 56[11], B3Vn.
	12 53 52.896	−60 23 06.78	−1.081	0.087	0.451	ESL 51[11], B3Vn.
				Interesting objects with *W12* < 0.05 but large *W23*		
NGC 4755	12 53 43.872	−60 22 28.76	−2.449	−0.030	1.769	CT Cru, Variable Star of β Cep type, $V_{\text{proj}} = 195\,\text{km s}^{-1}$[12], B1.5V
	12 53 48.177	−60 21 54.32	−1.779	−0.033	1.988	CPD-59 4556. Eclipsing binary (β Lyr type), B1V.
	12 53 51.729	−60 21 58.45	−2.010	−0.180	2.340	CX Cru, Variable Star of β Cep type, $V_{\text{proj}} = 278\,\text{km s}^{-1}$[12], B1V.

References: (1) Moffat & Vogt (1974), (2) Gushee (1919), (3) Huang & Gies (2006), (4) Marsh Boyer et al. (2012), (5) Huang et al. (2010), (6) Lavdovsky (1961), (7) McSwain & Gies (2005), (8) McSwain et al. (2009), (9) Wildey (1964), (10) Sanner et al. (2001), (11) Evans et al. (2005), (12) Hunter et al. (2009). All data available in SIMBAD astronomical database (Wenger et al. 2000).

Our selection of targets, stars that are likely OB MS cluster members, determined using the procedure described above, are shown as black and green symbols.

For the stars in each cluster, we used the empirical relations given by Yuan et al. (2013) for the extinction $A(W1) = 0.19 E(B–V)$ and color excess $E(W1 − W2) = 0.036 E(B–V)$, as well as the color excesses and distance modulus (μ_0) given by Kharchenko et al. (2013) to convert the observed $W1$ magnitude and $W1 − W2$ color to absolute magnitudes and intrinsic colors.

An error of 0.1 mag in $E(B − V)$, larger than the estimates given for the clusters under study, leads to a difference smaller than 0.004 mag in the determination of $W1 − W2$, while the typical observational error for this color is larger than 0.02 mag. The effect of such error in color excess in $WISE$ magnitudes is also small, particularly in comparison to the error of 0.275 mag introduced in the determination of cluster distances. However, these errors in the determination of μ_0 neither produce significant changes in the spectral type nor affect the main results of this work regarding the color excesses of Be stars.

The $WISE$ CMD for the clusters are presented in the right panels of Figures 1–5. The color of the points in these figures indicate different ranges of absolute J magnitude. From our models, we obtain that MS stars with effective temperatures between 10,000 and 30,000 K, corresponding to the B-type range, have absolute J magnitudes between −4 and 1: we subdivide this range in J magnitude as $−4 \leqslant J < −3$ (green points), $−3 \leqslant J < −2$ (blue points), $−2 \leqslant J < −1$ (magenta points), $−1 \leqslant J < 0$ (cyan points), and $0 \leq J < 1$ (yellow points). Red and black points with $J < −4$ correspond to O type stars and supergiants. Objects with $J > 1$ are indicated with black full circles. Open squares indicate the known Be stars. The Be nature of these objects has been previously determined either from spectroscopic observations (e.g., McSwain & Gies 2005; McSwain et al. 2009; Huang et al. 2010; Mathew & Subramaniam 2011; Marsh Boyer et al. 2012), or Hα narrow band photometry (e.g., Pigulski et al. 2001).

The $WISE$ CMD using all OB stars from the five open clusters (with absolute magnitude $J < 1$ and intrinsic color $J − H < 0.15$) is presented in Figure 6. Due to the low quality of the data of most objects with $W1 − W2 < −0.25$, we removed stars with $W1 − W2$ color beyond this limit, and this is why the B star sample is incomplete, particularly toward later spectral types. Stars with $W1 − W2 \geqslant 0.5$ are likely not MS B stars, but Class II young stellar objects (Koenig et al. 2012), so we removed them from the sample of B stars as well. Panel (a) of Figure 6 shows all the stars with gray points with error bars, and panel (b) highlights stars with a previous Be classification with colored squares. Full squares indicate stars of B spectral type (yellow, cyan, magenta, blue, and green points) and open squares correspond to earlier-type emission-line stars (red and black). This sample of B and Be stars will be analyzed in the following section.

Table 2 lists the 95 stars studied in this work with a previous Be classification. Their coordinates are tabulated in columns 1 and 2, their $WISE$ and 2MASS intrinsic magnitudes, colors, and errors are listed in columns 3–14, a number indicating the $WISE$ variability of the star in column 15 (0 where no variability flag could be assigned, 1 for stars that are stable, 2 for those without a clear variability signature, and 3 for stars that are variable). The spectral type (0 corresponds to B0, 1 to B1, and so on) and

luminosity class are indicated in columns 16 and 17, respectively, column 18 gives the name of the object as available in SIMBAD together with references relevant to the Be star classification of the object. In the last column, we give the Be class assigned to the object in this work, either early, mid, or late Be star.

3. Results

3.1. WISE CMD

Similar to Bonanos et al. (2010), we define *photometric Be stars* as B-type stars having color excesses within a certain range. In the case of *WISE* colors, Nikutta et al. (2014) defined *naked* stars as stellar objects without a protostellar dusty disk with $W1 − W2 < 0.8$. This limit prevents contamination from faint IR sources. For the whole group of *naked* stars not severely affected by extinction and dominated by MS or *normal* stars, objects with no evidence of a circumstellar disk, these authors find a mean value $\mu_{W_{12}} = −0.04$ for the color $W_{12} = W1 − W2$, with a standard deviation $\sigma_{W_{12}} = 0.03$.

For our sample of B stars with absolute J magnitude values between −4 and 1, the mean color is $\mu_{W_{12}} = −0.066$ with a standard deviation of $\sigma_{W_{12}} = 0.002$, whereas for the subgroup of early and mid B stars ($−4 < J < −1$), the values are $\mu_{W_{12}} = −0.023$ and $\sigma_{W_{12}} = 0.006$. We chose to use the conservative criteria given by Nikutta et al. (2014) according to which most *naked* or *normal* stars have $W1 − W2 < 0.05$. This limit is represented with a vertical black line in Figure 6(a) and represents the limit between stars behaving as the majority (or normal) and those B-type stars having an infrared excess.

Figure 6(b) shows all the stars in our sample of five clusters as gray circles and known Be stars as colored squares. As described before, different colors correspond to different J magnitude bins. We can see that Be stars cluster mainly in two regions of this plot, a large group is found together with *naked* or *normal* B stars in the region with $W1 − W2$ between −0.25 and 0.05, and another group in the region with $W1 − W2$ between 0.1 and 0.3.

Indeed, as can be seen in Figure 7, we find that 98.8% of the non-Be objects or *normal stars* have $W1 − W2 < 0.05$. We define Be star candidates as objects that have no Be star classification but have $W1 − W2 \geqslant 0.05$.

We split our sample of B stars in absolute magnitude bins corresponding to early ($−4 \leqslant J < −2$, green and blue points in Figure 6(b)), mid ($−2 \leqslant J < −1$, magenta points) and late B stars ($−1 \leqslant J < 1$ cyan and yellow points). Red and black points in Figure 6(b) correspond to O type stars and supergiants, with $J < −4$. The presence of B stars of luminosity class III could eventually pollute the different bins. However, as we do not expect to have a significant number of giants given the ages of the clusters under study, we do not take this possibility into account in the present article. This may be of interest when older clusters are studied.

Then, we have 144 early B stars of which 47 are known Be stars (32.6%). Among the 166 mid B stars, 33 are known Be stars (19.9%) and within the 836 late B stars, 15 (1.8%) are known Be stars. If we look at the early and mid B stars together, 25.8% are Be stars. The fraction of Be stars decreases significantly when the sample contains later type stars.

This dependency of the fraction of Be stars on the spectral type range under consideration has been extensively reported in the literature and is the reason why different authors find large Be fractions when observing the upper MS of open clusters

Table 4
Synthetic Infrared Magnitudes and Colors Computed for $n = 2$

$\rho_0/10^{-12}$	i	W1	W12	W23	J	H	K	$EW_{H\alpha}$	W1	W12	W23	J	H	K	$EW_{H\alpha}$	W1	W12	W23	J	H	K	$EW_{H\alpha}$
(g cm^{-3})	(°)	(mag)	(mag)	(mag)	(mag)	(mag)	(mag)	(Å)	(mag)	(mag)	(mag)	(mag)	(mag)	(mag)	(Å)	(mag)	(mag)	(mag)	(mag)	(mag)	(mag)	(Å)
								B1							B3							B7
100	18	−6.557	0.416	1.010	−5.519	−5.577	−5.996	−6.86	−4.924	0.332	0.834	−3.990	−4.114	−4.457	−10.47	−2.794	0.357	0.937	−1.853	−1.951	−2.343	−13.89
	45	−6.380	0.408	0.984	−5.366	−5.415	−5.825	−9.95	−4.721	0.326	0.831	−3.814	−3.930	−4.264	−18.2	−2.655	0.351	0.910	−1.722	−1.814	−2.209	−19.62
	60	−6.143	0.400	0.965	−5.163	−5.201	−5.596	−11.53	−4.474	0.323	0.836	−3.596	−3.703	−4.024	−23.92	−2.493	0.343	0.878	−1.577	−1.660	−2.055	−26.98
	72	−5.748	0.403	0.993	−4.806	−4.826	−5.198	−11.16	−4.103	0.333	0.882	−3.254	−3.344	−3.653	−23.13	−2.259	0.330	0.842	−1.381	−1.449	−1.834	−25.19
	84	−4.992	0.466	1.027	−3.950	−3.944	−4.348	−8.18	−3.514	0.400	0.986	−2.554	−2.622	−2.983	−20.41	−1.790	0.314	0.843	−0.989	−1.029	−1.383	−22.62
75	18	−6.206	0.437	1.104	−5.137	−5.207	−5.633	−9.61	−4.691	0.362	0.878	−3.692	−3.825	−4.189	−12.87	−2.526	0.361	0.973	−1.606	−1.705	−2.075	−14.7
	45	−6.046	0.430	1.074	−4.996	−5.058	−5.477	−14.21	−4.503	0.352	0.865	−3.529	−3.657	−4.011	−21.95	−2.383	0.357	0.950	−1.472	−1.565	−1.937	−20.75
	60	−5.835	0.423	1.045	−4.812	−4.865	−5.272	−17.01	−4.268	0.342	0.861	−3.330	−3.449	−3.790	−29.31	−2.218	0.350	0.921	−1.328	−1.411	−1.779	−28.86
	72	−5.478	0.420	1.042	−4.495	−4.533	−4.918	−16	−3.908	0.342	0.895	−3.019	−3.122	−3.441	−28.24	−1.981	0.338	0.886	−1.142	−1.209	−1.560	−27.31
	84	−4.715	0.479	1.104	−3.659	−3.673	−4.070	−13.76	−3.272	0.407	1.032	−2.323	−2.400	−2.739	−26.79	−1.518	0.319	0.879	−0.788	−0.824	−1.125	−23.77
50	18	−5.683	0.453	1.219	−4.605	−4.685	−5.108	−15.32	−4.311	0.406	0.999	−3.257	−3.391	−3.774	−16.63	−2.174	0.366	1.022	−1.292	−1.387	−1.726	−15.36
	45	−5.541	0.450	1.196	−4.477	−4.549	−4.968	−22.66	−4.147	0.397	0.968	−3.113	−3.243	−3.617	−27.99	−2.026	0.363	1.004	−1.160	−1.248	−1.582	−21.77
	60	−5.359	0.445	1.168	−4.315	−4.379	−4.789	−28.09	−3.942	0.385	0.939	−2.940	−3.063	−3.424	−37.79	−1.857	0.357	0.980	−1.025	−1.101	−1.423	−30.47
	72	−5.055	0.441	1.144	−4.048	−4.099	−4.490	−26.79	−3.620	0.371	0.934	−2.677	−2.786	−3.121	−36.74	−1.621	0.344	0.948	−0.861	−0.921	−1.213	−29.42
	84	−4.306	0.490	1.212	−3.272	−3.301	−3.676	−26.64	−2.951	0.416	1.079	−2.038	−2.117	−2.421	−36.43	−1.173	0.317	0.924	−0.570	−0.596	−0.818	−24.14
25	18	−4.758	0.463	1.334	−3.731	−3.799	−4.194	−30.51	−3.540	0.450	1.249	−2.511	−2.613	−2.985	−23.48	−1.614	0.378	1.100	−0.834	−0.903	−1.172	−15.45
	45	−4.641	0.461	1.325	−3.640	−3.698	−4.082	−46.06	−3.408	0.445	1.228	−2.413	−2.506	−2.862	−38.06	−1.466	0.373	1.090	−0.737	−0.794	−1.039	−22.61
	60	−4.496	0.458	1.312	−3.528	−3.574	−3.945	−57.27	−3.249	0.439	1.199	−2.296	−2.379	−2.715	−50.81	−1.300	0.363	1.074	−0.639	−0.684	−0.899	−31.29
	72	−4.268	0.453	1.295	−3.352	−3.385	−3.731	−60.1	−3.010	0.427	1.155	−2.127	−2.198	−2.498	−50.01	−1.085	0.338	1.042	−0.526	−0.557	−0.728	−31.7
	84	−3.644	0.468	1.318	−2.822	−2.829	−3.109	−54.52	−2.429	0.420	1.186	−1.702	−1.742	−1.955	−46.17	−0.703	0.279	0.968	−0.341	−0.344	−0.438	−23.22
10	18	−3.501	0.419	1.375	−2.972	−2.939	−3.105	−39.25	−2.349	0.425	1.393	−1.840	−1.822	−1.959	−27.6	−0.832	0.353	1.229	−0.464	−0.451	−0.535	−14.25
	45	−3.425	0.408	1.361	−2.934	−2.893	−3.047	−49.49	−2.264	0.411	1.378	−1.802	−1.776	−1.896	−44.24	−0.741	0.331	1.199	−0.430	−0.410	−0.473	−21.62
	60	−3.334	0.393	1.342	−2.887	−2.839	−2.977	−58.9	−2.164	0.393	1.360	−1.756	−1.724	−1.822	−57.53	−0.641	0.305	1.160	−0.393	−0.367	−0.406	−29.01
	72	−3.205	0.370	1.311	−2.814	−2.759	−2.877	−64.74	−2.026	0.367	1.330	−1.688	−1.650	−1.719	−59.93	−0.519	0.265	1.092	−0.345	−0.314	−0.326	−31.41
	84	−2.870	0.325	1.245	−2.592	−2.526	−2.599	−46.9	−1.723	0.311	1.235	−1.512	−1.466	−1.483	−45.67	−0.319	0.188	0.898	−0.252	−0.216	−0.193	−19.92
5	18	−2.794	0.236	1.202	−2.759	−2.662	−2.659	−23.17	−1.802	0.237	1.199	−1.716	−1.642	−1.656	−18.95	−0.459	0.196	1.095	−0.395	−0.342	−0.344	−10.29
	45	−2.754	0.222	1.170	−2.743	−2.642	−2.633	−21.65	−1.764	0.222	1.162	−1.702	−1.625	−1.631	−22.92	−0.421	0.179	1.046	−0.383	−0.328	−0.322	−13.37
	60	−2.711	0.206	1.129	−2.724	−2.620	−2.604	−22.2	−1.721	0.206	1.117	−1.685	−1.605	−1.603	−28.06	−0.379	0.160	0.989	−0.369	−0.312	−0.297	−17.61
	72	−2.653	0.188	1.065	−2.693	−2.586	−2.562	−22.65	−1.665	0.185	1.050	−1.658	−1.577	−1.565	−30.02	−0.328	0.136	0.904	−0.349	−0.291	−0.264	−19.61
	84	−2.509	0.153	0.923	−2.589	−2.480	−2.442	−13.34	−1.537	0.147	0.900	−1.576	−1.493	−1.465	−18.88	−0.237	0.100	0.714	−0.295	−0.237	−0.197	−10.33
2.5	18	−2.480	0.061	0.713	−2.687	−2.563	−2.494	−8.05	−1.525	0.071	0.701	−1.658	−1.562	−1.516	−8.31	−0.287	0.064	0.630	−0.370	−0.302	−0.271	−4.19
	45	−2.466	0.054	0.677	−2.681	−2.556	−2.485	−5.83	−1.512	0.064	0.666	−1.652	−1.556	−1.508	−7.07	−0.275	0.058	0.592	−0.365	−0.297	−0.264	−3.97
	60	−2.450	0.047	0.638	−2.673	−2.547	−2.474	−4.56	−1.497	0.057	0.626	−1.646	−1.548	−1.498	−7.11	−0.262	0.050	0.549	−0.360	−0.292	−0.256	−5.05
	72	−2.429	0.040	0.591	−2.659	−2.533	−2.458	−3.61	−1.479	0.050	0.578	−1.636	−1.537	−1.485	−6.97	−0.246	0.042	0.496	−0.353	−0.284	−0.245	−5.67
	84	−2.370	0.030	0.499	−2.609	−2.481	−2.404	−0.63	−1.433	0.041	0.488	−1.599	−1.500	−1.445	−2.15	−0.213	0.033	0.406	−0.329	−0.260	−0.217	−0.75
1	18	−2.366	−0.023	0.169	−2.658	−2.525	−2.436	0.08	−1.415	−0.009	0.177	−1.631	−1.527	−1.460	0.64	−0.209	0.000	0.163	−0.354	−0.281	−0.234	2.23
	45	−2.363	−0.024	0.156	−2.656	−2.523	−2.433	0.74	−1.412	−0.010	0.164	−1.630	−1.526	−1.458	1.49	−0.207	−0.001	0.152	−0.352	−0.280	−0.233	2.97
	60	−2.359	−0.025	0.144	−2.653	−2.520	−2.430	1.25	−1.409	−0.011	0.153	−1.627	−1.523	−1.456	1.99	−0.204	−0.002	0.142	−0.351	−0.278	−0.231	3.29
	72	−2.353	−0.027	0.132	−2.648	−2.515	−2.424	1.75	−1.404	−0.012	0.142	−1.624	−1.520	−1.452	2.43	−0.201	−0.003	0.132	−0.349	−0.276	−0.228	3.56
	84	−2.331	−0.028	0.114	−2.628	−2.494	−2.404	2.69	−1.389	−0.014	0.127	−1.610	−1.506	−1.437	4.07	−0.192	−0.004	0.120	−0.340	−0.267	−0.220	5.16

Table 5
Synthetic Infrared Magnitudes and Colors Computed for $n = 2.5$

$\rho_0/10^{-12}$	i	W1	W12	W23	J	H	K	$EW_{H\alpha}$	W1	W12	W23	J	H	K	$EW_{H\alpha}$	W1	W12	W23	J	H	K	$EW_{H\alpha}$
(g cm^{-3})	(°)	(mag)	(mag)	(mag)	(mag)	(mag)	(mag)	(Å)	(mag)	(mag)	(mag)	(mag)	(mag)	(mag)	(Å)	(mag)	(mag)	(mag)	(mag)	(mag)	(mag)	(Å)
					B1							B3							B7			
100	18	−5.163	0.359	1.030	−4.335	−4.413	−4.716	−15.09	−4.035	0.359	0.968	−3.171	−3.292	−3.578	−10.81	−2.110	0.323	0.913	−1.338	−1.436	−1.713	−8.67
	45	−4.981	0.360	1.033	−4.153	−4.229	−4.531	−22.28	−3.845	0.359	0.953	−2.980	−3.100	−3.384	−17.35	−1.931	0.321	0.903	−1.167	−1.260	−1.536	−12.13
	60	−4.763	0.362	1.038	−3.941	−4.012	−4.310	−30.51	−3.619	0.357	0.934	−2.761	−2.878	−3.158	−25.74	−1.726	0.318	0.888	−0.986	−1.070	−1.337	−18.07
	72	−4.438	0.367	1.053	−3.635	−3.695	−3.983	−36.92	−3.290	0.353	0.920	−2.460	−2.566	−2.833	−29.14	−1.445	0.309	0.869	−0.778	−0.843	−1.078	−20.28
	84	−3.686	0.419	1.157	−2.893	−2.925	−3.183	−38.32	−2.585	0.385	1.033	−1.815	−1.887	−2.111	−31.34	−0.952	0.282	0.852	−0.465	−0.490	−0.645	−14.59
75	18	−4.867	0.353	1.038	−4.076	−4.147	−4.436	−17.29	−3.765	0.362	1.029	−2.927	−3.038	−3.317	−12.32	−1.915	0.323	0.936	−1.172	−1.264	−1.524	−9.01
	45	−4.688	0.355	1.044	−3.897	−3.965	−4.253	−24.77	−3.580	0.364	1.023	−2.741	−2.851	−3.128	−19.01	−1.734	0.322	0.930	−1.003	−1.089	−1.344	−12.71
	60	−4.474	0.356	1.052	−3.692	−3.755	−4.038	−33.78	−3.364	0.365	1.012	−2.532	−2.638	−2.909	−27.93	−1.528	0.319	0.919	−0.832	−0.907	−1.147	−18.73
	72	−4.163	0.360	1.072	−3.406	−3.458	−3.727	−41.87	−3.055	0.364	0.998	−2.256	−2.349	−2.604	−32.26	−1.252	0.307	0.902	−0.647	−0.703	−0.901	−21.43
	84	−3.450	0.398	1.169	−2.762	−2.779	−2.996	−39.82	−2.384	0.379	1.070	−1.703	−1.756	−1.943	−31.32	−0.786	0.267	0.866	−0.386	−0.402	−0.513	−14.18
50	18	−4.464	0.342	1.033	−3.726	−3.787	−4.057	−19.92	−3.376	0.353	1.064	−2.597	−2.688	−2.953	−14.25	−1.652	0.322	0.965	−0.957	−1.037	−1.272	−9.1
	45	−4.289	0.344	1.041	−3.560	−3.614	−3.881	−26.36	−3.193	0.356	1.070	−2.424	−2.510	−2.767	−21.05	−1.469	0.322	0.963	−0.800	−0.870	−1.091	−12.91
	60	−4.084	0.345	1.051	−3.373	−3.418	−3.676	−34.79	−2.983	0.359	1.074	−2.234	−2.312	−2.557	−30.2	−1.264	0.318	0.956	−0.652	−0.709	−0.902	−18.71
	72	−3.792	0.347	1.071	−3.131	−3.159	−3.393	−42.79	−2.693	0.360	1.075	−2.001	−2.063	−2.276	−35.43	−1.002	0.298	0.940	−0.502	−0.540	−0.683	−21.85
	84	−3.148	0.353	1.146	−2.640	−2.628	−2.781	−34.84	−2.100	0.351	1.099	−1.591	−1.609	−1.733	−29.54	−0.587	0.237	0.867	−0.307	−0.308	−0.365	−13.13
25	18	−3.771	0.320	1.003	−3.170	−3.186	−3.403	−19.73	−2.666	0.331	1.045	−2.046	−2.083	−2.285	−13.86	−1.193	0.319	0.996	−0.633	−0.671	−0.840	−7.61
	45	−3.609	0.318	1.008	−3.059	−3.058	−3.254	−20.96	−2.487	0.329	1.060	−1.931	−1.952	−2.124	−18.44	−1.016	0.313	0.999	−0.530	−0.554	−0.687	−10.55
	60	−3.425	0.313	1.013	−2.941	−2.925	−3.092	−24.35	−2.287	0.324	1.076	−1.811	−1.817	−1.951	−24.96	−0.830	0.297	0.995	−0.439	−0.449	−0.541	−15.05
	72	−3.184	0.296	1.015	−2.801	−2.768	−2.893	−27.58	−2.038	0.307	1.086	−1.679	−1.668	−1.748	−29.34	−0.620	0.259	0.962	−0.351	−0.348	−0.390	−17.95
	84	−2.736	0.243	0.981	−2.553	−2.489	−2.533	−17.43	−1.632	0.248	1.031	−1.477	−1.438	−1.437	−19.04	−0.333	0.177	0.806	−0.240	−0.216	−0.200	−9.24
10	18	−2.910	0.248	0.950	−2.788	−2.705	−2.731	−8.79	−1.905	0.250	0.955	−1.740	−1.679	−1.718	−7.14	−0.579	0.236	0.962	−0.417	−0.379	−0.407	−3.28
	45	−2.811	0.222	0.925	−2.749	−2.657	−2.664	−7.36	−1.806	0.222	0.923	−1.704	−1.635	−1.653	−6.98	−0.484	0.206	0.925	−0.386	−0.341	−0.348	−4.08
	60	−2.713	0.190	0.882	−2.710	−2.611	−2.600	−7.03	−1.707	0.189	0.875	−1.667	−1.593	−1.590	−8.13	−0.394	0.171	0.870	−0.357	−0.307	−0.293	−6.03
	72	−2.610	0.152	0.799	−2.665	−2.560	−2.532	−6.75	−1.603	0.147	0.793	−1.626	−1.548	−1.523	−8.95	−0.305	0.130	0.772	−0.325	−0.273	−0.239	−7.31
	84	−2.448	0.096	0.624	−2.579	−2.468	−2.418	−3.27	−1.459	0.090	0.618	−1.559	−1.475	−1.427	−3.52	−0.204	0.079	0.567	−0.280	−0.224	−0.175	−1.84
5	18	−2.535	0.095	0.735	−2.698	−2.579	−2.521	−3.2	−1.577	0.102	0.727	−1.668	−1.576	−1.543	−2.2	−0.326	0.096	0.698	−0.374	−0.311	−0.287	0.18
	45	−2.493	0.074	0.667	−2.683	−2.561	−2.496	−1.95	−1.538	0.082	0.656	−1.655	−1.561	−1.519	−1.35	−0.290	0.076	0.622	−0.363	−0.298	−0.266	0.43
	60	−2.456	0.055	0.588	−2.668	−2.543	−2.473	−1.24	−1.503	0.063	0.575	−1.642	−1.546	−1.498	−1.22	−0.257	0.057	0.539	−0.353	−0.286	−0.247	−0.03
	72	−2.421	0.039	0.493	−2.649	−2.523	−2.448	−0.59	−1.470	0.047	0.478	−1.626	−1.529	−1.476	−1.04	−0.227	0.039	0.440	−0.341	−0.273	−0.229	−0.28
	84	−2.362	0.018	0.352	−2.608	−2.481	−2.402	0.9	−1.422	0.027	0.341	−1.597	−1.499	−1.441	1.42	−0.192	0.023	0.310	−0.321	−0.253	−0.204	2.45
2.5	18	−2.397	0.000	0.343	−2.666	−2.536	−2.452	−0.09	−1.444	0.013	0.342	−1.638	−1.537	−1.475	0.86	−0.233	0.020	0.325	−0.359	−0.288	−0.246	2.63
	45	−2.384	−0.007	0.291	−2.660	−2.529	−2.443	0.68	−1.432	0.006	0.290	−1.634	−1.531	−1.468	1.58	−0.223	0.013	0.275	−0.355	−0.283	−0.240	3.14
	60	−2.372	−0.013	0.245	−2.654	−2.522	−2.435	1.21	−1.421	0.001	0.245	−1.629	−1.526	−1.461	1.98	−0.213	0.008	0.230	−0.351	−0.279	−0.234	3.29
	72	−2.359	−0.017	0.203	−2.645	−2.513	−2.425	1.73	−1.411	−0.003	0.205	−1.622	−1.519	−1.453	2.37	−0.204	0.004	0.191	−0.347	−0.275	−0.228	3.49
	84	−2.336	−0.021	0.147	−2.626	−2.493	−2.404	2.56	−1.394	−0.007	0.154	−1.609	−1.505	−1.438	3.7	−0.193	0.001	0.146	−0.338	−0.266	−0.218	4.86
1	18	−2.349	−0.035	0.051	−2.652	−2.518	−2.426	2.06	−1.400	−0.020	0.069	−1.626	−1.521	−1.452	2.91	−0.197	−0.009	0.075	−0.350	−0.277	−0.228	4.47
	45	−2.346	−0.036	0.038	−2.650	−2.516	−2.423	2.39	−1.397	−0.021	0.057	−1.625	−1.520	−1.450	3.3	−0.195	−0.010	0.065	−0.349	−0.276	−0.226	4.83
	60	−2.342	−0.037	0.029	−2.648	−2.513	−2.421	2.67	−1.394	−0.022	0.048	−1.623	−1.518	−1.448	3.59	−0.193	−0.010	0.057	−0.348	−0.274	−0.225	5.07
	72	−2.339	−0.037	0.021	−2.644	−2.510	−2.417	2.97	−1.392	−0.022	0.042	−1.621	−1.516	−1.445	3.91	−0.191	−0.011	0.052	−0.347	−0.273	−0.224	5.33
	84	−2.330	−0.038	0.014	−2.636	−2.502	−2.409	3.35	−1.386	−0.023	0.036	−1.615	−1.510	−1.440	4.47	−0.188	−0.011	0.047	−0.343	−0.270	−0.220	6.06

Table 6
Synthetic Infrared Magnitudes and Colors Computed for $n = 3$

$\rho_0/10^{-12}$	i	$W1$	$W12$	$W23$	J	H	K	EW$_{H\alpha}$	$W1$	$W12$	$W23$	J	H	K	EW$_{H\alpha}$	$W1$	$W12$	$W23$	J	H	K	EW$_{H\alpha}$
(g cm^{-3})	(°)	(mag)	(mag)	(mag)	(mag)	(mag)	(mag)	(Å)	(mag)	(mag)	(mag)	(mag)	(mag)	(mag)	(Å)	(mag)	(mag)	(mag)	(mag)	(mag)	(mag)	(Å)
					B1							B3							B7			
100	18	−4.343	0.264	0.806	−3.786	−3.829	−4.027	−9.74	−3.285	0.281	0.871	−2.683	−2.761	−2.948	−6.74	−1.700	0.282	0.851	−1.079	−1.160	−1.362	−4.43
	45	−4.132	0.266	0.815	−3.579	−3.618	−3.814	−11.52	−3.067	0.285	0.883	−2.467	−2.543	−2.726	−8.8	−1.495	0.282	0.853	−0.887	−0.963	−1.159	−6.34
	60	−3.886	0.267	0.828	−3.347	−3.380	−3.570	−15.03	−2.818	0.288	0.897	−2.229	−2.300	−2.475	−13.13	−1.264	0.280	0.851	−0.697	−0.761	−0.937	−9.89
	72	−3.546	0.268	0.853	−3.052	−3.070	−3.238	−19.19	−2.483	0.291	0.914	−1.942	−1.996	−2.147	−17.45	−0.966	0.265	0.844	−0.509	−0.551	−0.677	−12.7
	84	−2.882	0.258	0.917	−2.579	−2.548	−2.628	−13.18	−1.877	0.275	0.940	−1.537	−1.540	−1.602	−11.31	−0.531	0.206	0.767	−0.298	−0.299	−0.337	−5.47
75	18	−4.132	0.255	0.792	−3.613	−3.645	−3.832	−8.97	−3.062	0.267	0.846	−2.507	−2.570	−2.746	−6.21	−1.543	0.279	0.858	−0.954	−1.027	−1.215	−3.77
	45	−3.924	0.256	0.800	−3.412	−3.439	−3.624	−10.47	−2.842	0.270	0.860	−2.296	−2.356	−2.525	−8.23	−1.336	0.279	0.861	−0.768	−0.833	−1.011	−5.59
	60	−3.684	0.257	0.811	−3.193	−3.211	−3.386	−13.51	−2.591	0.272	0.875	−2.071	−2.122	−2.277	−12.2	−1.106	0.275	0.861	−0.595	−0.646	−0.795	−8.82
	72	−3.356	0.254	0.831	−2.933	−2.931	−3.075	−16.73	−2.261	0.271	0.895	−1.818	−1.849	−1.964	−16	−0.822	0.254	0.850	−0.436	−0.465	−0.559	−11.31
	84	−2.762	0.222	0.850	−2.557	−2.508	−2.559	−10.44	−1.714	0.233	0.887	−1.500	−1.482	−1.502	−8.95	−0.430	0.183	0.740	−0.268	−0.259	−0.270	−4.25
50	18	−3.838	0.243	0.773	−3.368	−3.386	−3.559	−8	−2.762	0.248	0.805	−2.266	−2.311	−2.474	−5.27	−1.324	0.270	0.853	−0.791	−0.847	−1.014	−2.61
	45	−3.635	0.243	0.780	−3.185	−3.192	−3.358	−8.77	−2.541	0.248	0.820	−2.075	−2.108	−2.257	−6.89	−1.117	0.269	0.858	−0.625	−0.668	−0.814	−4.17
	60	−3.404	0.242	0.788	−2.998	−2.989	−3.136	−10.7	−2.292	0.247	0.837	−1.883	−1.901	−2.020	−9.96	−0.892	0.261	0.859	−0.484	−0.510	−0.616	−6.87
	72	−3.103	0.230	0.797	−2.799	−2.768	−2.870	−12.43	−1.980	0.235	0.855	−1.691	−1.687	−1.749	−12.6	−0.636	0.228	0.837	−0.362	−0.370	−0.420	−8.84
	84	−2.630	0.172	0.743	−2.548	−2.476	−2.492	−7.01	−1.543	0.173	0.787	−1.481	−1.436	−1.412	−5.83	−0.318	0.148	0.684	−0.245	−0.222	−0.204	−2.53
25	18	−3.329	0.228	0.743	−2.980	−2.954	−3.079	−5.76	−2.288	0.231	0.746	−1.910	−1.904	−2.030	−3.51	−0.937	0.247	0.806	−0.551	−0.561	−0.673	−0.61
	45	−3.142	0.221	0.745	−2.867	−2.820	−2.915	−5.23	−2.088	0.222	0.753	−1.798	−1.772	−1.860	−3.84	−0.744	0.235	0.808	−0.452	−0.445	−0.516	−1.37
	60	−2.945	0.204	0.741	−2.765	−2.700	−2.759	−5.41	−1.881	0.200	0.755	−1.698	−1.656	−1.700	−5.07	−0.560	0.206	0.795	−0.375	−0.355	−0.383	−2.98
	72	−2.736	0.165	0.700	−2.669	−2.589	−2.606	−5.39	−1.665	0.157	0.722	−1.608	−1.552	−1.547	−5.93	−0.383	0.156	0.730	−0.311	−0.281	−0.268	−4.06
	84	−2.476	0.096	0.541	−2.561	−2.460	−2.427	−2.52	−1.437	0.090	0.557	−1.519	−1.445	−1.395	−1.6	−0.210	0.087	0.525	−0.253	−0.209	−0.163	0.29
10	18	−2.700	0.162	0.697	−2.734	−2.632	−2.612	−2.04	−1.733	0.165	0.699	−1.703	−1.626	−1.628	−0.61	−0.451	0.158	0.705	−0.397	−0.346	−0.349	1.61
	45	−2.597	0.126	0.653	−2.698	−2.587	−2.547	−1.17	−1.634	0.130	0.646	−1.669	−1.585	−1.566	−0.09	−0.358	0.121	0.643	−0.369	−0.312	−0.293	1.78
	60	−2.514	0.090	0.574	−2.668	−2.551	−2.496	−0.7	−1.553	0.093	0.561	−1.641	−1.552	−1.517	−0.06	−0.283	0.084	0.553	−0.346	−0.285	−0.250	1.45
	72	−2.445	0.057	0.456	−2.639	−2.519	−2.452	−0.18	−1.486	0.059	0.440	−1.616	−1.525	−1.477	0.11	−0.225	0.051	0.429	−0.326	−0.263	−0.217	1.33
	84	−2.367	0.020	0.296	−2.601	−2.477	−2.401	1.09	−1.417	0.025	0.287	−1.587	−1.493	−1.434	1.97	−0.178	0.023	0.275	−0.307	−0.242	−0.189	3.33
5	18	−2.458	0.044	0.504	−2.679	−2.554	−2.482	0.03	−1.504	0.054	0.501	−1.651	−1.554	−1.505	1.2	−0.278	0.056	0.482	−0.367	−0.299	−0.266	3.05
	45	−2.419	0.023	0.415	−2.665	−2.537	−2.459	0.75	−1.468	0.033	0.411	−1.639	−1.540	−1.484	1.77	−0.244	0.036	0.391	−0.356	−0.287	−0.247	3.42
	60	−2.391	0.007	0.325	−2.653	−2.524	−2.441	1.23	−1.441	0.018	0.322	−1.629	−1.528	−1.468	2.06	−0.220	0.020	0.301	−0.348	−0.278	−0.233	3.49
	72	−2.369	−0.004	0.244	−2.641	−2.511	−2.426	1.73	−1.422	0.008	0.242	−1.620	−1.518	−1.455	2.41	−0.202	0.010	0.222	−0.341	−0.270	−0.222	3.67
	84	−2.342	−0.015	0.149	−2.623	−2.492	−2.405	2.5	−1.400	−0.003	0.155	−1.607	−1.505	−1.439	3.34	−0.187	0.001	0.146	−0.332	−0.261	−0.211	4.8
2.5	18	−2.373	−0.017	0.208	−2.659	−2.527	−2.439	1.43	−1.423	−0.002	0.216	−1.633	−1.529	−1.464	2.43	−0.217	0.007	0.212	−0.355	−0.283	−0.238	4.11
	45	−2.361	−0.023	0.153	−2.653	−2.520	−2.431	1.94	−1.411	−0.009	0.162	−1.628	−1.524	−1.457	2.9	−0.207	0.001	0.161	−0.352	−0.279	−0.232	4.48
	60	−2.352	−0.027	0.114	−2.648	−2.515	−2.424	2.32	−1.403	−0.013	0.125	−1.624	−1.520	−1.452	3.22	−0.200	−0.003	0.125	−0.349	−0.276	−0.228	4.68
	72	−2.344	−0.030	0.087	−2.643	−2.509	−2.418	2.7	−1.397	−0.016	0.099	−1.620	−1.516	−1.447	3.56	−0.195	−0.006	0.101	−0.346	−0.273	−0.224	4.93
	84	−2.334	−0.032	0.054	−2.634	−2.500	−2.409	3.16	−1.389	−0.018	0.070	−1.614	−1.509	−1.440	4.13	−0.190	−0.007	0.076	−0.342	−0.269	−0.220	5.64
1	18	−2.344	−0.038	0.019	−2.650	−2.515	−2.423	2.5	−1.395	−0.023	0.040	−1.624	−1.519	−1.449	3.4	−0.194	−0.011	0.051	−0.349	−0.276	−0.226	4.97
	45	−2.341	−0.039	0.007	−2.648	−2.513	−2.420	2.76	−1.393	−0.024	0.029	−1.623	−1.518	−1.447	3.68	−0.192	−0.012	0.041	−0.348	−0.274	−0.225	5.23
	60	−2.338	−0.039	0.000	−2.646	−2.511	−2.418	2.97	−1.391	−0.024	0.022	−1.622	−1.517	−1.446	3.9	−0.190	−0.012	0.036	−0.347	−0.274	−0.224	5.42
	72	−2.336	−0.040	−0.004	−2.644	−2.509	−2.416	3.19	−1.389	−0.025	0.019	−1.620	−1.515	−1.444	4.15	−0.189	−0.013	0.032	−0.346	−0.273	−0.223	5.64
	84	−2.332	−0.040	−0.008	−2.640	−2.505	−2.412	3.31	−1.386	−0.025	0.015	−1.618	−1.512	−1.442	4.45	−0.187	−0.013	0.030	−0.345	−0.271	−0.221	6.08

Table 7
Synthetic Infrared Magnitudes and Colors Computed for $n = 3.5$

$\rho_0/10^{-12}$	i	$W1$	$W12$	$W23$	J	H	K	$EW_{H\alpha}$	$W1$	$W12$	$W23$	J	H	K	$EW_{H\alpha}$	$W1$	$W12$	$W23$	J	H	K	$EW_{H\alpha}$
(g cm^{-3})	(°)	(mag)	(mag)	(mag)	(mag)	(mag)	(mag)	(Å)	(mag)	(mag)	(mag)	(mag)	(mag)	(mag)	(Å)	(mag)	(mag)	(mag)	(mag)	(mag)	(mag)	(Å)
					B1							B3							B7			
100	18	−3.890	0.199	0.633	−3.511	−3.521	−3.659	−4.01	−2.825	0.203	0.663	−2.422	−2.463	−2.585	−2.04	−1.420	0.239	0.748	−0.926	−0.988	−1.139	−0.34
	45	−3.664	0.200	0.640	−3.294	−3.299	−3.433	−4.62	−2.581	0.203	0.676	−2.194	−2.230	−2.344	−2.97	−1.197	0.238	0.752	−0.725	−0.779	−0.920	−1.35
	60	−3.406	0.198	0.649	−3.062	−3.057	−3.181	−5.98	−2.307	0.202	0.691	−1.953	−1.979	−2.077	−4.89	−0.949	0.233	0.753	−0.540	−0.578	−0.689	−3.14
	72	−3.069	0.191	0.660	−2.811	−2.783	−2.870	−7.17	−1.958	0.194	0.707	−1.708	−1.709	−1.759	−6.59	−0.658	0.205	0.737	−0.384	−0.400	−0.453	−4.43
	84	−2.582	0.135	0.596	−2.547	−2.473	−2.475	−3.81	−1.508	0.134	0.627	−1.483	−1.438	−1.405	−1.91	−0.318	0.129	0.586	−0.252	−0.231	−0.213	0.33
75	18	−3.726	0.192	0.622	−3.378	−3.378	−3.506	−3.64	−2.663	0.193	0.639	−2.293	−2.322	−2.439	−1.67	−1.286	0.230	0.731	−0.829	−0.880	−1.020	0.2
	45	−3.503	0.192	0.629	−3.169	−3.161	−3.285	−4.03	−2.422	0.192	0.652	−2.074	−2.095	−2.202	−2.47	−1.063	0.228	0.734	−0.637	−0.677	−0.802	−0.67
	60	−3.251	0.190	0.635	−2.955	−2.934	−3.042	−4.98	−2.152	0.189	0.667	−1.855	−1.862	−1.944	−4.06	−0.820	0.220	0.734	−0.474	−0.497	−0.584	−2.21
	72	−2.935	0.175	0.638	−2.747	−2.702	−2.765	−5.59	−1.823	0.171	0.678	−1.654	−1.636	−1.662	−5.24	−0.551	0.183	0.706	−0.346	−0.349	−0.378	−3.22
	84	−2.529	0.111	0.533	−2.550	−2.465	−2.452	−2.66	−1.453	0.106	0.562	−1.488	−1.431	−1.385	−1.03	−0.264	0.106	0.532	−0.246	−0.218	−0.186	1.05
50	18	−3.494	0.183	0.608	−3.185	−3.174	−3.290	−3.16	−2.451	0.182	0.609	−2.115	−2.127	−2.242	−1.19	−1.101	0.215	0.694	−0.700	−0.733	−0.857	0.93
	45	−3.275	0.182	0.613	−2.999	−2.972	−3.077	−3.16	−2.216	0.179	0.621	−1.922	−1.920	−2.015	−1.66	−0.879	0.211	0.697	−0.534	−0.550	−0.647	0.36
	60	−3.035	0.176	0.615	−2.828	−2.781	−2.856	−3.55	−1.959	0.171	0.632	−1.751	−1.729	−1.785	−2.69	−0.648	0.194	0.692	−0.407	−0.407	−0.457	−0.78
	72	−2.765	0.146	0.593	−2.682	−2.613	−2.640	−3.57	−1.680	0.137	0.619	−1.612	−1.569	−1.568	−3.28	−0.422	0.147	0.639	−0.315	−0.297	−0.297	−1.45
	84	−2.468	0.080	0.445	−2.558	−2.460	−2.427	−1.12	−1.416	0.074	0.465	−1.509	−1.438	−1.384	0.08	−0.212	0.076	0.444	−0.250	−0.210	−0.167	2
25	18	−3.087	0.173	0.585	−2.887	−2.836	−2.907	−2	−2.093	0.178	0.578	−1.845	−1.816	−1.901	−0.26	−0.777	0.191	0.627	−0.509	−0.500	−0.578	1.97
	45	−2.888	0.162	0.584	−2.779	−2.705	−2.741	−1.47	−1.888	0.163	0.576	−1.739	−1.689	−1.734	−0.09	−0.578	0.172	0.622	−0.416	−0.389	−0.423	1.94
	60	−2.701	0.133	0.563	−2.695	−2.604	−2.603	−1.24	−1.698	0.130	0.555	−1.658	−1.594	−1.597	−0.34	−0.407	0.132	0.586	−0.351	−0.313	−0.307	1.47
	72	−2.542	0.087	0.472	−2.631	−2.529	−2.497	−0.82	−1.537	0.081	0.467	−1.599	−1.524	−1.492	−0.3	−0.272	0.082	0.478	−0.306	−0.260	−0.224	1.28
	84	−2.394	0.035	0.305	−2.579	−2.464	−2.403	0.72	−1.407	0.034	0.308	−1.555	−1.469	−1.411	1.65	−0.174	0.037	0.299	−0.277	−0.222	−0.169	3.34
10	18	−2.600	0.113	0.547	−2.710	−2.599	−2.557	−0.04	−1.645	0.119	0.551	−1.684	−1.599	−1.581	1.26	−0.390	0.116	0.551	−0.390	−0.332	−0.322	3.19
	45	−2.501	0.074	0.485	−2.677	−2.558	−2.497	0.62	−1.549	0.080	0.482	−1.653	−1.561	−1.524	1.74	−0.301	0.077	0.472	−0.362	−0.299	−0.270	3.49
	60	−2.434	0.040	0.383	−2.653	−2.529	−2.457	1.05	−1.485	0.048	0.377	−1.631	−1.535	−1.486	1.95	−0.241	0.044	0.364	−0.344	−0.278	−0.236	3.5
	72	−2.389	0.016	0.273	−2.634	−2.508	−2.429	1.54	−1.442	0.024	0.267	−1.614	−1.517	−1.460	2.27	−0.203	0.021	0.254	−0.331	−0.264	−0.214	3.67
	84	−2.346	−0.007	0.157	−2.615	−2.486	−2.402	2.31	−1.403	0.003	0.159	−1.599	−1.500	−1.437	3.15	−0.176	0.004	0.156	−0.321	−0.252	−0.199	4.69
5	18	−2.423	0.020	0.376	−2.670	−2.542	−2.464	1.14	−1.473	0.032	0.378	−1.645	−1.545	−1.489	2.26	−0.257	0.037	0.368	−0.363	−0.294	−0.257	4.02
	45	−2.388	−0.001	0.278	−2.658	−2.527	−2.443	1.69	−1.439	0.012	0.280	−1.633	−1.531	−1.470	2.72	−0.226	0.018	0.271	−0.354	−0.283	−0.240	4.35
	60	−2.366	−0.013	0.196	−2.648	−2.517	−2.429	2.09	−1.418	0.000	0.199	−1.625	−1.522	−1.457	3.01	−0.207	0.007	0.191	−0.347	−0.276	−0.229	4.5
	72	−2.352	−0.019	0.135	−2.640	−2.508	−2.419	2.51	−1.406	−0.006	0.143	−1.618	−1.515	−1.449	3.35	−0.196	0.000	0.137	−0.342	−0.270	−0.222	4.75
	84	−2.337	−0.027	0.073	−2.631	−2.498	−2.408	2.96	−1.393	−0.013	0.086	−1.611	−1.508	−1.440	3.9	−0.187	−0.005	0.088	−0.338	−0.266	−0.216	5.41
2.5	18	−2.363	−0.024	0.143	−2.656	−2.523	−2.433	1.99	−1.412	−0.010	0.155	−1.629	−1.526	−1.458	2.99	−0.210	0.001	0.158	−0.353	−0.281	−0.234	4.64
	45	−2.351	−0.030	0.090	−2.650	−2.517	−2.426	2.4	−1.402	−0.016	0.104	−1.625	−1.521	−1.452	3.36	−0.201	−0.005	0.111	−0.350	−0.277	−0.229	4.94
	60	−2.345	−0.033	0.060	−2.646	−2.512	−2.421	2.71	−1.397	−0.019	0.075	−1.622	−1.518	−1.448	3.63	−0.195	−0.008	0.083	−0.348	−0.274	−0.226	5.13
	72	−2.339	−0.035	0.041	−2.642	−2.508	−2.416	3.01	−1.393	−0.020	0.058	−1.620	−1.515	−1.445	3.92	−0.192	−0.009	0.067	−0.346	−0.272	−0.223	5.37
	84	−2.334	−0.036	0.020	−2.638	−2.504	−2.411	3.23	−1.388	−0.021	0.040	−1.616	−1.511	−1.441	4.27	−0.189	−0.010	0.051	−0.343	−0.270	−0.221	5.82
1	18	−2.341	−0.039	0.005	−2.649	−2.514	−2.421	2.69	−1.393	−0.024	0.027	−1.624	−1.519	−1.448	3.61	−0.193	−0.012	0.040	−0.349	−0.275	−0.226	5.18
	45	−2.338	−0.040	−0.006	−2.646	−2.512	−2.419	2.91	−1.391	−0.025	0.017	−1.622	−1.517	−1.446	3.84	−0.190	−0.013	0.032	−0.348	−0.274	−0.224	5.39
	60	−2.337	−0.040	−0.011	−2.645	−2.511	−2.417	3.08	−1.390	−0.025	0.012	−1.621	−1.516	−1.445	4.03	−0.190	−0.013	0.027	−0.347	−0.273	−0.223	5.55
	72	−2.335	−0.040	−0.014	−2.644	−2.509	−2.416	3.22	−1.388	−0.025	0.010	−1.620	−1.515	−1.444	4.22	−0.189	−0.013	0.025	−0.346	−0.273	−0.223	5.74
	84	−2.333	−0.041	−0.016	−2.642	−2.507	−2.414	3.26	−1.387	−0.026	0.008	−1.619	−1.513	−1.442	4.34	−0.187	−0.014	0.023	−0.345	−0.272	−0.222	6.03

Table 8
Synthetic Infrared Magnitudes and Colors Computed for $n = 4$

$\rho_0/10^{-12}$	i	W1	W12	W23	J	H	K	EW$_{H\alpha}$	W1	W12	W23	J	H	K	EW$_{H\alpha}$	W1	W12	W23	J	H	K	EW$_{H\alpha}$
(g cm^{-3})	(°)	(mag)	(mag)	(mag)	(mag)	(mag)	(mag)	(Å)	(mag)	(mag)	(mag)	(mag)	(mag)	(mag)	(Å)	(mag)	(mag)	(mag)	(mag)	(mag)	(mag)	(Å)
					B1							B3							B7			
100	18	−3.601	0.157	0.520	−3.341	−3.327	−3.424	−1.85	−2.555	0.154	0.523	−2.274	−2.289	−2.376	−0.11	−1.220	0.196	0.621	−0.832	−0.875	−0.991	1.59
	45	−3.365	0.156	0.525	−3.120	−3.100	−3.192	−2.03	−2.301	0.152	0.535	−2.042	−2.051	−2.127	−0.53	−0.984	0.193	0.621	−0.626	−0.659	−0.762	1.16
	60	−3.103	0.153	0.530	−2.896	−2.862	−2.939	−2.52	−2.021	0.148	0.547	−1.813	−1.807	−1.860	−1.41	−0.728	0.183	0.617	−0.453	−0.468	−0.533	0.35
	72	−2.790	0.132	0.520	−2.700	−2.640	−2.670	−2.61	−1.698	0.123	0.547	−1.623	−1.592	−1.590	−1.85	−0.462	0.140	0.574	−0.330	−0.324	−0.333	−0.04
	84	−2.464	0.070	0.385	−2.555	−2.460	−2.427	−0.33	−1.406	0.064	0.407	−1.501	−1.433	−1.377	0.89	−0.221	0.071	0.392	−0.251	−0.215	−0.174	2.88
75	18	−3.465	0.151	0.511	−3.232	−3.210	−3.298	−1.61	−2.433	0.149	0.507	−2.172	−2.177	−2.262	0.12	−1.106	0.186	0.596	−0.752	−0.785	−0.891	1.93
	45	−3.233	0.150	0.516	−3.019	−2.988	−3.070	−1.67	−2.184	0.145	0.517	−1.952	−1.947	−2.021	−0.19	−0.871	0.182	0.596	−0.559	−0.578	−0.666	1.62
	60	−2.977	0.145	0.518	−2.822	−2.772	−2.830	−1.94	−1.912	0.139	0.527	−1.752	−1.729	−1.770	−0.84	−0.625	0.167	0.589	−0.411	−0.411	−0.456	0.98
	72	−2.698	0.114	0.489	−2.667	−2.594	−2.605	−1.79	−1.626	0.104	0.508	−1.604	−1.558	−1.544	−1.03	−0.389	0.118	0.527	−0.312	−0.294	−0.287	0.75
	84	−2.435	0.054	0.339	−2.561	−2.459	−2.417	0.28	−1.394	0.049	0.357	−1.515	−1.440	−1.381	1.32	−0.196	0.055	0.343	−0.255	−0.213	−0.166	3.26
50	18	−3.273	0.144	0.500	−3.074	−3.042	−3.120	−1.26	−2.268	0.144	0.489	−2.028	−2.020	−2.106	0.44	−0.950	0.172	0.560	−0.645	−0.661	−0.755	2.37
	45	−3.046	0.142	0.502	−2.888	−2.838	−2.900	−1.08	−2.028	0.139	0.495	−1.839	−1.813	−1.877	0.36	−0.718	0.165	0.559	−0.482	−0.479	−0.542	2.26
	60	−2.807	0.129	0.498	−2.740	−2.668	−2.694	−1.06	−1.778	0.123	0.496	−1.692	−1.646	−1.666	0.02	−0.494	0.139	0.542	−0.371	−0.351	−0.367	1.85
	72	−2.588	0.087	0.433	−2.636	−2.547	−2.531	−0.69	−1.555	0.079	0.438	−1.594	−1.531	−1.504	0.08	−0.308	0.088	0.452	−0.302	−0.268	−0.243	1.77
	84	−2.401	0.034	0.278	−2.571	−2.461	−2.406	0.98	−1.392	0.032	0.289	−1.538	−1.456	−1.396	1.9	−0.176	0.037	0.279	−0.266	−0.216	−0.165	3.73
25	18	−2.937	0.137	0.480	−2.834	−2.767	−2.805	−0.44	−1.971	0.144	0.476	−1.807	−1.763	−1.821	1.06	−0.676	0.155	0.509	−0.484	−0.464	−0.519	3.07
	45	−2.734	0.122	0.475	−2.732	−2.641	−2.641	0.07	−1.766	0.125	0.468	−1.707	−1.642	−1.659	1.36	−0.477	0.129	0.496	−0.398	−0.357	−0.369	3.24
	60	−2.568	0.084	0.431	−2.664	−2.560	−2.526	0.4	−1.599	0.085	0.422	−1.642	−1.565	−1.546	1.41	−0.327	0.086	0.437	−0.343	−0.295	−0.272	3.14
	72	−2.454	0.045	0.320	−2.621	−2.508	−2.452	0.88	−1.485	0.044	0.311	−1.601	−1.517	−1.474	1.68	−0.229	0.044	0.316	−0.311	−0.257	−0.213	3.25
	84	−2.362	0.007	0.186	−2.592	−2.471	−2.398	1.88	−1.401	0.012	0.189	−1.575	−1.483	−1.423	2.81	−0.167	0.015	0.188	−0.294	−0.234	−0.179	4.45
10	18	−2.543	0.082	0.447	−2.697	−2.580	−2.527	0.87	−1.590	0.090	0.454	−1.671	−1.582	−1.552	2.08	−0.354	0.092	0.454	−0.385	−0.323	−0.307	3.91
	45	−2.449	0.041	0.371	−2.666	−2.542	−2.471	1.42	−1.501	0.051	0.372	−1.644	−1.547	−1.500	2.51	−0.270	0.052	0.363	−0.359	−0.292	−0.257	4.22
	60	−2.396	0.013	0.263	−2.647	−2.520	−2.440	1.82	−1.451	0.023	0.263	−1.626	−1.527	−1.470	2.77	−0.223	0.024	0.253	−0.344	−0.276	−0.231	4.33
	72	−2.366	−0.004	0.175	−2.634	−2.505	−2.421	2.26	−1.422	0.007	0.177	−1.615	−1.515	−1.453	3.1	−0.197	0.009	0.168	−0.335	−0.266	−0.216	4.56
	84	−2.338	−0.020	0.091	−2.623	−2.492	−2.404	2.73	−1.396	−0.008	0.101	−1.605	−1.504	−1.438	3.68	−0.179	−0.003	0.102	−0.328	−0.259	−0.206	5.23
5	18	−2.404	0.006	0.296	−2.666	−2.536	−2.454	1.67	−1.452	0.019	0.301	−1.639	−1.538	−1.478	2.75	−0.244	0.029	0.297	−0.361	−0.291	−0.252	4.47
	45	−2.371	−0.013	0.195	−2.654	−2.522	−2.434	2.14	−1.422	0.000	0.202	−1.629	−1.526	−1.461	3.15	−0.216	0.009	0.201	−0.353	−0.281	−0.235	4.77
	60	−2.355	−0.022	0.125	−2.646	−2.513	−2.424	2.49	−1.407	−0.009	0.134	−1.623	−1.519	−1.452	3.42	−0.202	0.000	0.135	−0.347	−0.275	−0.227	4.94
	72	−2.345	−0.027	0.081	−2.640	−2.507	−2.417	2.84	−1.399	−0.013	0.093	−1.618	−1.514	−1.446	3.73	−0.194	−0.004	0.097	−0.344	−0.271	−0.222	5.19
	84	−2.335	−0.032	0.038	−2.635	−2.501	−2.410	3.08	−1.391	−0.018	0.054	−1.614	−1.510	−1.441	4.08	−0.188	−0.008	0.062	−0.341	−0.268	−0.218	5.63
2.5	18	−2.357	−0.028	0.106	−2.654	−2.521	−2.430	2.27	−1.408	−0.013	0.120	−1.629	−1.524	−1.456	3.26	−0.206	−0.003	0.127	−0.353	−0.280	−0.232	4.9
	45	−2.347	−0.034	0.056	−2.649	−2.515	−2.423	2.63	−1.398	−0.019	0.073	−1.624	−1.519	−1.450	3.58	−0.197	−0.007	0.082	−0.350	−0.276	−0.228	5.16
	60	−2.341	−0.036	0.032	−2.645	−2.511	−2.419	2.89	−1.394	−0.021	0.050	−1.622	−1.517	−1.447	3.83	−0.193	−0.010	0.062	−0.348	−0.274	−0.225	5.34
	72	−2.337	−0.037	0.019	−2.643	−2.508	−2.416	3.13	−1.391	−0.022	0.039	−1.620	−1.515	−1.444	4.07	−0.191	−0.011	0.051	−0.346	−0.273	−0.223	5.56
	84	−2.334	−0.038	0.004	−2.640	−2.505	−2.413	3.22	−1.388	−0.023	0.025	−1.618	−1.513	−1.442	4.24	−0.189	−0.011	0.039	−0.344	−0.271	−0.221	5.87
1	18	−2.341	−0.040	−0.003	−2.649	−2.514	−2.421	2.79	−1.393	−0.025	0.020	−1.624	−1.519	−1.448	3.72	−0.192	−0.012	0.034	−0.349	−0.276	−0.226	5.29
	45	−2.338	−0.040	−0.012	−2.646	−2.512	−2.418	2.99	−1.390	−0.025	0.011	−1.622	−1.517	−1.446	3.93	−0.190	−0.013	0.026	−0.348	−0.274	−0.224	5.47
	60	−2.336	−0.041	−0.016	−2.645	−2.510	−2.417	3.13	−1.389	−0.026	0.007	−1.621	−1.516	−1.445	4.09	−0.189	−0.014	0.023	−0.347	−0.273	−0.223	5.61
	72	−2.335	−0.041	−0.018	−2.644	−2.509	−2.416	3.21	−1.388	−0.026	0.006	−1.621	−1.515	−1.444	4.23	−0.189	−0.014	0.022	−0.347	−0.273	−0.223	5.77
	84	−2.333	−0.041	−0.020	−2.642	−2.508	−2.414	3.23	−1.387	−0.026	0.004	−1.619	−1.514	−1.443	4.27	−0.188	−0.014	0.020	−0.346	−0.272	−0.222	5.94
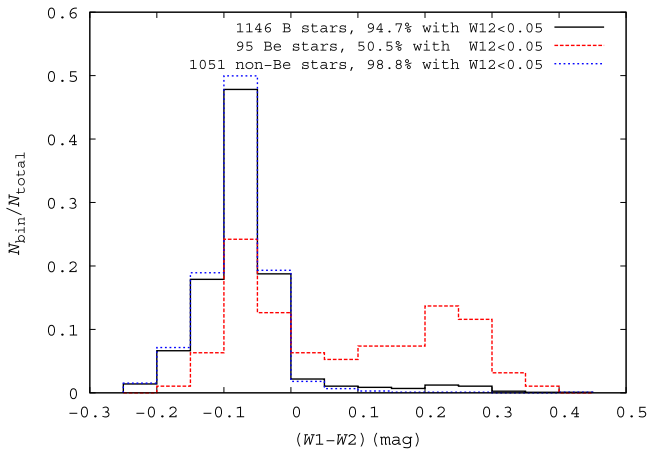
Figure 7. Fraction of stars in each $W1 - W2$ color bin. The black continuous line shows the distribution of all B stars in our sample, the red line shows the distribution of Be stars and the blue line shows the distribution of objects that are not known to be Be stars.
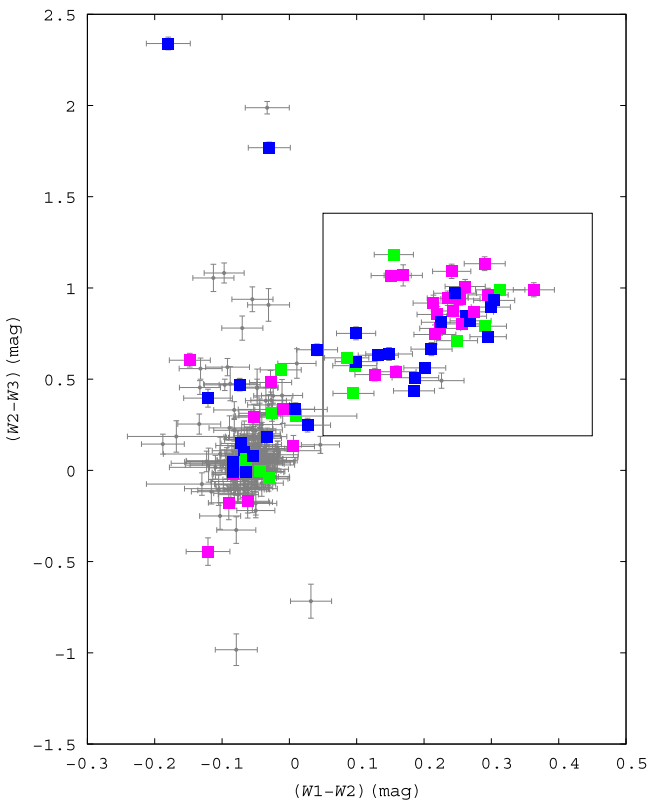
Figure 8. Color–color diagram $W2 - W3$ vs. $W1 - W2$ for mid and early B stars. The quality of $W3$ band of late B-type stars is usually poor so we did not consider these objects. Gray points indicate all early and mid B-type stars. Colored symbols indicate Be stars. The region occupied by Be stars in an active phase, $W1 - W2 \geqslant 0.05$, is indicated with a black rectangle.

(e.g., Grebel et al. 1992; Grebel 1997; Maeder et al. 1999; Keller et al. 2001; McSwain & Gies 2005; Martayan et al. 2010; Iqbal & Keller 2013). These works do not properly account for the late B and Be-type stars.

When looking at our overall sample ($-4 < J < 1$), the fraction of Be stars is 8.5%. Because of the lack of completeness, in particular of the late B-type sample, the proportion of Be stars might certainly be lower for the whole B sample.

Of all early Be stars, 49% have $W1 - W2 \geqslant 0.05$; among mid Be stars, the percentage increases to 60.6% and, for late Be stars. decreases to 26.7%. The number of Be candidates in our sample is 1 in the early Be group, 1 in the mid Be group, and 12 in the late Be group.

In the mid and early Be star groups, 43 out of the 45 stars with an excess $W1 - W2 \geqslant 0.05$ are known Be stars (95.6%). We assume that we know all the Be stars in these spectral ranges, for the open clusters studied in this article. This indicates that there may remain only a few objects to be discovered as mid and early Be stars within these clusters.

On the contrary, in the late Be group, the large proportion of new candidates indicates that, for late B stars, the classification as Be stars can be more difficult and a significant number of these objects may have eluded a previous detection. In Table 3, we list the coordinates, absolute $W1$ magnitude, $W1 - W2$ (indicated as $W12$), $W2 - W3$ (indicated as $W23$), and other relevant data for all the Be candidates and other interesting objects as well.

The presence of a circumstellar disk may not always be evident if the disk is not dense or large enough and/or the spectroscopic observations are not done with sufficient resolution. In this sense, the *WISE* photometric classification can identify new targets to look for the Be phenomenon, which could be studied later spectroscopically.

Figure 8 represents the *WISE* color–color diagram $W2 - W3$ versus $W1 - W2$. We included only early and mid B-type stars because of the low quality of $W3$ for most of late B-type stars. All Be stars with $W1 - W2 > 0.05$ reside within a well determined region, indicated as a black rectangle in the plot. Most Be stars with $W1 - W2 < 0.05$ behave as normal B stars, most of which have $W2 - W3 < 0.6$, with the remarkable exception of two Be stars with $W2 - W3 > 1.5$, and a third non-Be star. These very red colors are definitely not character-istic of Be stars, and interestingly both stars are not only Be stars but also have a β Cephei classification. The non-Be star that behaves similarly to these two objects is an eclipsing binary. The colors of these objects agree with those presented by Nikutta et al. (2014) for a central star with a temperature of 10,000 K surrounded by an optically thin dusty shell with a rather flat density distribution. This kind of density profile places more dust at large radial distances, where the temperature is lower. In this case, a small increase in optical depth can significantly enhance long wavelength emission and therefore increasing $W2 - W3$ while having a value of close to 0 for the warmer color $W1 - W2$. This observable signature could be evidence of the β Cephei behavior, as pulsations could enhance the shifting of dust at large radial distances. All three objects deserve further study. The coordinates and other characteristics of both Be stars and the third interesting star are listed in Table 3.

3.2. WISE Variability of Be Stars

In order to probe the variability of our sample of Be stars, we investigate the variability flags given in the ALLWISE catalog (Cutri et al. 2013). Figure 9 shows the *WISE* CMD for all Be stars in our sample. The different symbols and colors represent Be stars that have different variability flags in their *WISE* magnitudes (Hoffman et al. 2012).

As explained in the AllWISE data release,[5] the AllWISE source catalog contains one set of calibrated magnitudes per object. With this aim, during the AllWISE science data

---

[5] http://wise2.ipac.caltech.edu/docs/release/allwise
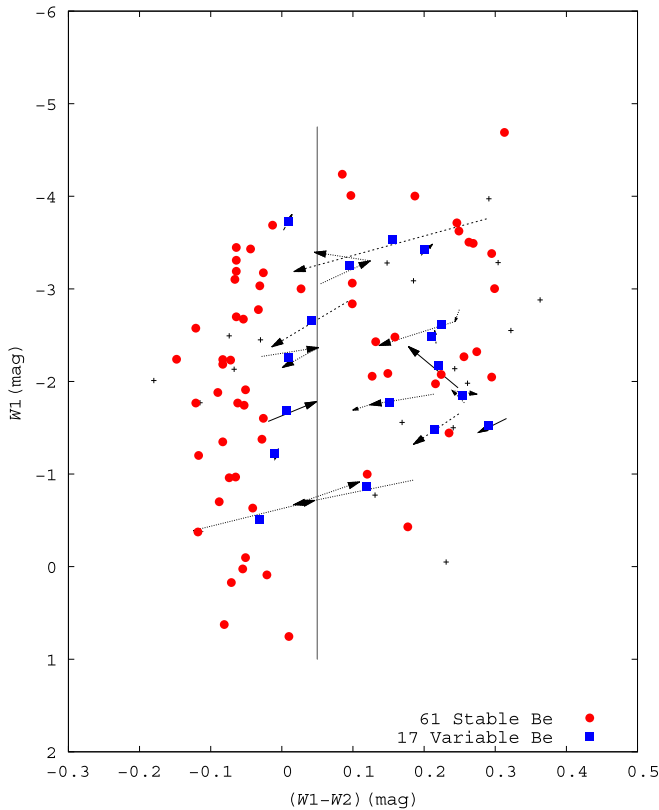
Figure 9. CMD of Be stars. The different colors indicate different *WISE* variability flags: Red circles indicate stable Be stars while blue squares correspond to objects that are variable objects. The remaining stars do not have a clear variability signature or have low quality data so a variability flag could not be identified. The arrows indicate the extent of variability between different observing epochs of the blue squares.

Figure 10. Cumulative distribution of stable and variable Be stars. The two samples are unlikely to come from the same distribution , because the the Kolmogorov–Smirnov statistic (D_{max}) is larger than the corresponding critical value for the two-sample Kolmogorov–Smirnov test (D_{crit}).

processing, single-exposure images obtained in different epochs were coadded, allowing the detection of sources and the measurement of the position, apparent motion and photometry for each of them. Profile-fit photometry was performed simultaneously in the four *WISE* bands, and also for each filter and single-exposure image, so not only one set of calibrated magnitudes per object was obtained, but also multiepoch photometry is available for each object and in each band. During this data processing, flux variability in a band was evaluated by analyzing the distribution of flux measurements of a source on the individual single-exposure frames, and hence a variability flag was assigned to each band.

Because the clusters under study are near the Galactic plane, the single-exposure images from which the observations of the Be stars presented in our article originate were performed in either two or three different epochs, separated by around 180 days. In each epoch, 10 to 16 individual observations were obtained within two to five days, all of them available in the AllWISE Multiepoch Photometry Database.[6]

In Figure 9, the red circles indicate Be stars with variability flags compatible with no variation (flags 0–5) while blue squares correspond to objects that are very likely variable objects (flags 8–9). For the remaining objects, identified with black crosses, either the quality of the data did not allow any variability flag to be provided in *W1* or *W2* bands, or the

---

[6] http://wise2.ipac.caltech.edu/docs/release/allwise/expsup/sec3_1.html

variability flags did not provide a clear variability signature (flag 6 or 7).

We see that red and blue symbols occupy different regions of the CMD: while the 61 non-variable Be stars tend to reside either with the *normal* B stars, or with stars with a significant excess, the 17 variable Be stars tend to occupy a transition region between *normal* B stars and stars having a significant excess.

By doing a two-sample Kolmogorov–Smirnov test of these variable and non-variable Be stars, we find that it is unlikely that these two samples come from the same distribution, as shown in Figure 10. The null hypothesis that both samples come from a population with the same distribution can be rejected at a significance level of $\alpha = 0.005$.

We interpret the differences between the two samples in the *WISE* CMD in terms of quiescent (*normal* B) and active phases, in which the star hosts a circumstellar disk. A lack of variability is found either for Be stars in a quiescent (diskless phase), or for stars that have a developed disk that is not changing significantly. On the other hand, variable stars are Be stars undergoing disk changes. Among the 95 Be stars of our sample, 17 are definitely variable stars, with light and color changes observed during the 18 months of *WISE* observations. This constitutes 18% of the sample.

To show the variability of the Be stars flagged as variables, we calculated the mean *W1* and *W2* magnitudes for each epoch and plotted the corresponding data in Figure 9. The variability between consecutive epochs is indicated with an arrow pointing in the direction of the time evolution. The six variable stars that are in the quiescent state undergo small color and magnitude changes, indicating that some minor mass loss episodes could occur in these objects. There is a significant change in color and magnitude in most of the variable active stars.

As described in the following section, the variability observed in the most active variable Be stars is compatible with a disk dissipation phase. In order to interpret the nature of the variability behavior of Be stars, we have generated synthetic *WISE* colors using the BERAY circumstellar disk code (Sigut 2011).
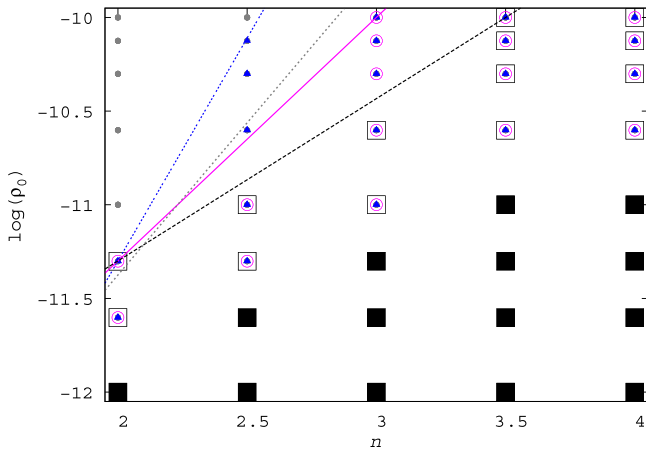
Figure 11. ρ_0 vs. n plot for our disk models for an intermediate inclination angle of 60 degrees. Small gray full circles correspond to models that do not describe the observed $W1 - W2$ colors for any spectral type, blue triangles show the combinations of parameters that describe early-type Be stars, magenta open circles correspond to intermediate-type stars, and black open squares correspond to late-type Be stars. The black full squares correspond to models with $W1 - W2 < 0.05$. The blue, magenta, and black lines describe the limits for each spectral type. The thin gray line indicates the limit of the *forbidden zone* as described by Vieira et al. (2017).

4. Disk Model Predictions

In order to obtain the IR continuum flux of B1, B3, and B7 spectral type stars[7] hosting circumstellar disks, we used the codes BEDISK (Sigut & Jones 2007) and BERAY (Sigut 2011). The former computes the temperature structure for a given disk density structure; the statistical equilibrium equations are solved to obtain the atomic level populations used for computation of the heating and cooling rates, which are balanced to fix the temperature. The latter solves the radiative transfer equation along 10^5 rays through the star-plus-disk system for a given inclination angle. Rays that terminate on the stellar surface use an appropriately limb-darkened intensity for the boundary condition on the transfer equation. In this way, different observables can be computed, such as line profiles, spectral energy distributions (SEDs), or monochromatic images projected on the sky. These codes have been broadly used for the interpretation of Hα lines (Silaj et al. 2010; Ahmed & Sigut 2012; Sigut & Patel 2013; Silaj et al. 2014), near-IR spectroscopy (Jones et al. 2009), and interferometric observations (Jones et al. 2008; Tycner et al. 2008; Sigut et al. 2015) of Be star disks. In the present work, SEDs are the focus of the modeling as these can be used to compute the required near-IR magnitudes and colors.

For the present work, we use an axisymmetric disk density distribution in which the radial density depends on two parameters: ρ_0, the density at the base of the disk, and n, the power-law exponent that determines how the density decreases with distance in the equatorial plane from the star. The disk density distribution in the cyclindrical coordinates (R, Z) is

$$\rho(R, Z) = \rho_0 \left(\frac{r_0}{R}\right)^n e^{-\left(\frac{Z}{H}\right)^2}. \qquad (1)$$

Here, r_0 is the stellar radius and H is the disk scale height, computed assuming the disk is in hydrostatic equilibrium in the vertical (i.e., Z) direction with an isothermal temperature of

---

[7] The stellar parameters for these spectral types are taken from Cox (2000), consistent with previous work of the authors.
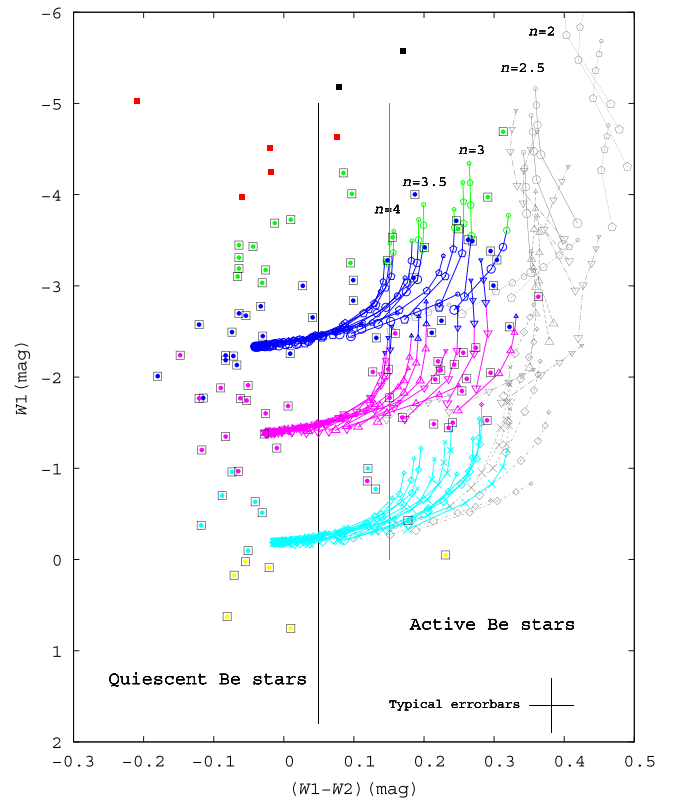
Figure 12. Emission line stars along with synthetic points in the *WISE* CMD obtained with BEDISK/BERAY. Full colored symbols indicate emission-line stars, those surrounded by a black square indicate classical Be stars. The black line separates active Be stars (with $W1 - W2 \geqslant 0.05$) from quiescent Be stars. Circles, hexagons, triangles, crosses, and diamonds indicate models with different combinations of n and ρ computed with BEDISK/BERAY. The gray symbols correspond to combinations of n and ρ that are unlikely to be found in Be stars, following Vieira et al. (2017). Families of models with different n for early B stars are indicated in the plot.

$0.6\, T_{\rm eff}$ (see Sigut et al. 2009). This isothermal temperature is used only to fix the disk scale height and this, coupled with the assumption of vertical hydrostatic equilibrium, produces a flaring disk with $H \propto R^{3/2}$.

We computed SEDs assuming different values of ρ_0, between 10^{-12} and 10^{-10} g cm^{-3}, and for different values of n, ranging between 2 and 4. These are typical values often considered for Be stars in the literature (Rivinius et al. 2013). For the present calculations, we considered a disk size of 50 stellar radii, and a variety of inclination angles.

For each model, we computed *WISE* magnitudes by convolving our synthetic energy distributions with each *WISE* filter, as described by Jarrett et al. (2011). We also obtained 2MASS J magnitudes by using 2MASS filter definitions and the fluxes for zero magnitude from Cohen et al. (2003). We present the computed magnitudes (*W1, J, H, K*) and *WISE* colors (*W1 − W2* indicated as *W12* and *W2 − W3* indicated as *W23*) for three different spectral types for five different values of n, eight values of ρ_0, and five different inclination angles in Tables 4–7 and 8. In addition, we also provide for each model the predicted equivalent width of the Hα line (EW$_{H\alpha}$), a quantity of special interest for Be stars as emission in the Balmer series (i.e., a negative value of EW$_{H\alpha}$) is the defining characteristic of the Be stars and a signature of disk emission.
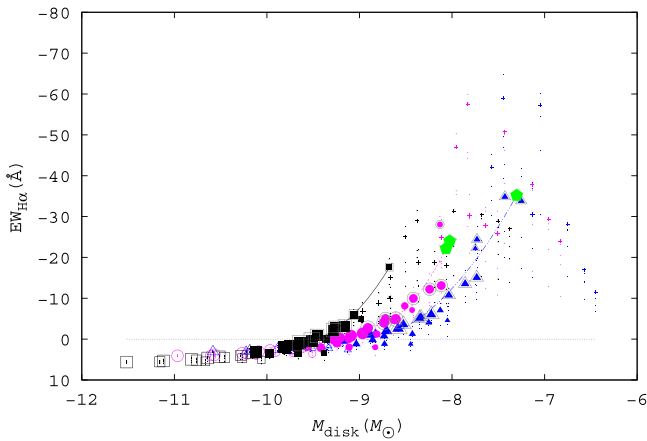
Figure 13. Hα equivalent width vs. disk mass. Small dots indicate models for all five inclinations given in this article. All bigger symbols correspond to an inclination angle of 60°. Blue triangles show the values for early B-type models, magenta circles for intermediate mass, and black squares for late B-type stars. Open symbols indicate forbidden models with $W1 - W2 < 0.05$ and small crosses indicate models that produce large colors not observed for cluster Be stars. Gray symbols indicate those models with $W1 - W2 \geqslant 0.15$, and the colored curves are second-order polynomial fits to these points. The gray horizontal line separates emission (negative values) and absorption (positive values) Hα lines. The green symbols identify the three stars with available Hα spectroscopy.

4.1. Allowed n and ρ_0 for Be Stars

From Figure 6, we see that the late-type Be stars and candidates have $W1 - W2 < 0.25$, whereas the mid- and early B-type objects have $W1 - W2 < 0.35$. We now explore our models to see which combinations of ρ_0 and n give $W1 - W2$ compatible with these limits.

Figure 11 shows, for an inclination of 60°, which combinations of the disk density parameters ρ_0 and n are consistent with the above limits. The blue, magenta, and black lines describe the limits for early, mid, and late spectral types, respectively. There is a clear trend with spectral type: larger ρ_0 base densities are allowed for smaller n for earlier spectral types, indicating that earlier spectra types can have more massive disks. Changing the inclination angle changes these limits somewhat, particularly larger inclination angles where the disk is projected against the stellar surface, but the overall trend with spectral type is not modified. The limits here agree with disk density *forbidden zone* as described by Vieira et al. (2017) (shown in the figure as a gray line), obtained for a large sample of Be stars with different inclination angles. Finally, the open squares indicate the combinations of parameters that lead to $W1 - W2 < 0.05$, thus appearing as normal B stars.

In Figure 12, we plot the known Be stars (squares with a black central point) for the five open clusters, together with the synthetic colors and magnitudes in the *W1* versus $W1 - W2$ color–magnitude diagram (gray symbols and colored circles). Once more, the different colors indicate different *J* magnitude ranges. The gray symbols correspond to models with combinations of n and ρ_0 that are outside the usual range of parameters found when fitting Be star disk models, called the *forbidden region* by Vieira et al. (2017). Circles and hexagons correspond to models with an early-type central stars, triangles to mid B central stars and crosses and diamonds to late B-type stars. The different shapes help to distinguish models with different n, and different symbol sizes correspond to different viewing angles. We see that there are no Be stars in the region

Table 9
Disk Masses

n	$\rho_0/10^{-12}$ g cm^{-3}	B1 (13.2$M_\odot$)	B3 (7.6$M_\odot$) $M_d[M_*]$	B7 (4.2$M_\odot$)
2	100	2.74×10^{-8}	1.95×10^{-8}	9.97×10^{-9}
2	75	2.05×10^{-8}	1.46×10^{-8}	7.47×10^{-9}
2	50	1.37×10^{-8}	9.74×10^{-9}	4.98×10^{-9}
2	25	6.84×10^{-9}	4.87×10^{-9}	2.49×10^{-9}
2	10	2.74×10^{-9}	1.95×10^{-9}	9.97×10^{-10}
2	5	1.37×10^{-9}	9.74×10^{-10}	4.98×10^{-10}
2	2.5	6.84×10^{-10}	4.87×10^{-10}	2.49×10^{-10}
2	1	2.74×10^{-10}	1.95×10^{-10}	9.97×10^{-11}
2.5	100	5.71×10^{-9}	4.06×10^{-9}	2.08×10^{-9}
2.5	75	4.28×10^{-9}	3.05×10^{-9}	1.56×10^{-9}
2.5	50	2.85×10^{-9}	2.03×10^{-9}	1.04×10^{-9}
2.5	25	1.43×10^{-9}	1.02×10^{-9}	5.19×10^{-10}
2.5	10	5.71×10^{-10}	4.06×10^{-10}	2.08×10^{-10}
2.5	5	2.85×10^{-10}	2.03×10^{-10}	1.04×10^{-10}
2.5	2.5	1.43×10^{-10}	1.02×10^{-10}	5.19×10^{-11}
2.5	1	5.71×10^{-11}	4.06×10^{-11}	2.08×10^{-11}
3	100	1.41×10^{-9}	1.01×10^{-9}	5.15×10^{-10}
3	75	1.06×10^{-9}	7.55×10^{-10}	3.86×10^{-10}
3	50	7.07×10^{-10}	5.03×10^{-10}	2.57×10^{-10}
3	25	3.54×10^{-10}	2.52×10^{-10}	1.29×10^{-10}
3	10	1.41×10^{-10}	1.01×10^{-10}	5.15×10^{-11}
3	5	7.07×10^{-11}	5.03×10^{-11}	2.57×10^{-11}
3	2.5	3.54×10^{-11}	2.52×10^{-11}	1.29×10^{-11}
3	1	1.41×10^{-11}	1.01×10^{-11}	5.15×10^{-12}
3.5	100	4.56×10^{-10}	3.24×10^{-10}	1.66×10^{-10}
3.5	75	3.42×10^{-10}	2.43×10^{-10}	1.24×10^{-10}
3.5	50	2.28×10^{-10}	1.62×10^{-10}	8.29×10^{-11}
3.5	25	1.14×10^{-10}	8.11×10^{-11}	4.15×10^{-11}
3.5	10	4.56×10^{-11}	3.24×10^{-11}	1.66×10^{-11}
3.5	5	2.28×10^{-11}	1.62×10^{-11}	8.29×10^{-12}
3.5	2.5	1.14×10^{-11}	8.11×10^{-12}	4.15×10^{-12}
3.5	1	4.56×10^{-12}	3.24×10^{-12}	1.66×10^{-12}
4	100	2.00×10^{-10}	1.42×10^{-10}	7.28×10^{-11}
4	75	1.50×10^{-10}	1.07×10^{-10}	5.46×10^{-11}
4	50	1.00×10^{-10}	7.12×10^{-11}	3.64×10^{-11}
4	25	5.00×10^{-11}	3.56×10^{-11}	1.82×10^{-11}
4	10	2.00×10^{-11}	1.42×10^{-11}	7.28×10^{-12}
4	5	1.00×10^{-11}	7.12×10^{-12}	3.64×10^{-12}
4	2.5	5.00×10^{-12}	3.56×10^{-12}	1.82×10^{-12}
4	1	2.00×10^{-12}	1.42×10^{-12}	7.28×10^{-13}

of the CMD occupied by the forbidden models, indicating that indeed these kinds of more massive disks do not correspond to MS Be stars. The computed models are seen to nicely cover the region occupied by Be stars and to correctly describe their corresponding *J* magnitudes. The models with the smallest disks (lowest ρ_0) are located in the region of *normal* B stars or very close to it. With increasing ρ_0, the effect of inclination becomes more prominent, as discussed in the next section.

4.2. Effects of the Inclination Angle

In Figure 12, identical disk models but with different viewing inclination angles of 18° (smallest symbols), 45°, 60°, 72°, and 84° (largest symbols) are connected with a continuous line. For a fixed stellar mass, the models with the smallest n have more massive disks for the same ρ_0 and have redder colors. Interestingly, the analysis of near-IR photometry of Be
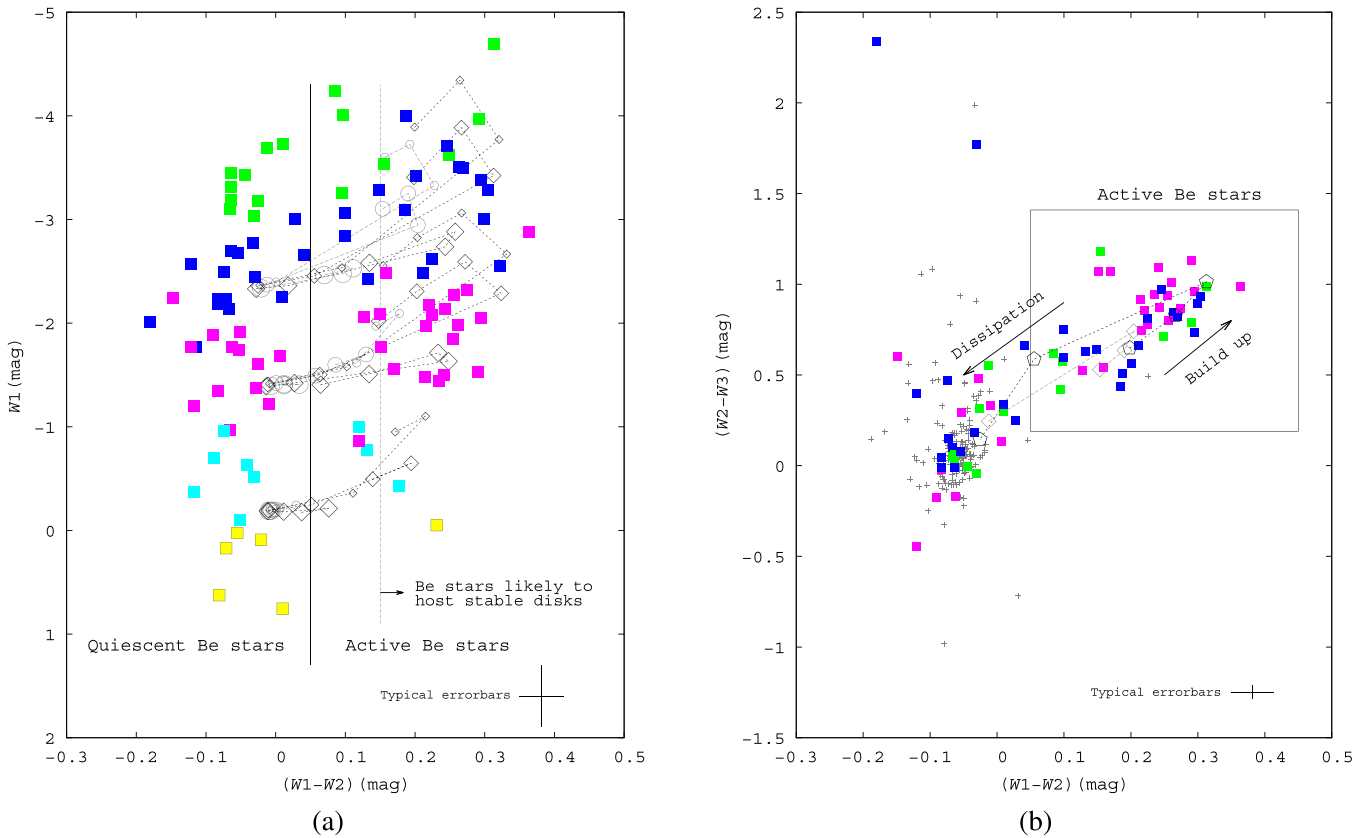
Figure 14. Be stars shown together with the modeled loops predicted during disk formation and dissipation phases in the color–magnitude (a) and color–color (b) diagrams. The color coding is the same as in previous plots. We see in (a) that, except for systems with a large inclination angle, the direction of the loop is clockwise. Our modeling shows that active Be stars with $W1 - W2 \geqslant 0.15$ are likely to have stable developed disks. The loops shown correspond to the three different spectral types and three inclination angles. Panel (b) shows only early- and mid-type B stars in the color–color diagram, and the predicted loop for mid B-type stars with an inclination angle of $60°$. In this case, the direction of the loop is counterclockwise. The black crosses indicate all non-Be objects.

stars has the potential of being useful to study whether there is a preferential viewing angle in stellar clusters, as has already been found in certain clusters (Corsaro et al. 2017). According to our results, we expect that clusters with preferred pole-on inclinations and Be stars with developed disks, with $W1 - W2 \geqslant 0.15$, have $W1$ magnitudes around one magnitude brighter than those clusters with preferential equator-on inclinations.

4.3. Mass of the Disk and its Relation to the Hα Equivalent Width

By integrating our model disk densities over the volume of the disk to radial distance of 50 stellar radii, we obtain an estimate of the mass of the disk. Table 9 provides the disk mass for each model in units of the stellar mass (M_*). The assumed stellar mass for each spectral type is indicated on top of each column, so conversion to solar masses is straightforward. Figure 13 shows the Hα equivalent width (EW) versus the corresponding model disk mass (in $M_\odot$) for different spectral types and disk density parameters, all for an inclination angle of $60°$. Models with other inclination angles are indicated with dots, for ease of comparison. Small crosses correspond to combinations of parameters that belong to the disk density forbidden region. The color coding in Figure 13 is the same as in Figure 11: black squares correspond to late B stars, magenta circles to intermediate B stars, and blue triangles to early

B stars. The point size is proportional to the value of n, the smallest correspond to $n = 2$ and the largest, to $n = 4$.

We find that the early-type models can have more massive disks and produce larger Hα equivalent widths than the later B-type models, in agreement with Arcos et al. (2017). Open symbols indicate objects with $W1 - W2 < 0.05$, the region typically occupied by normal B stars. Interestingly, all these models have positive EW, indicating that these objects do not have a significant disk emission contribution to the photospheric Hα line. Full symbols correspond to models with $W1 - W2$ below the forbidden region limit and $W1 - W2 \geqslant 0.05$. It is remarkable that, for a fixed inclination angle and spectral type of the central star, there is a one-to-one relation between EW and the mass of the disk, particularly for those models with large color excess. We discuss this later in the context of stars with stable, developed disks. The one-to-one relation for the three spectral types and an inclination angle of $60°$ is represented by colored lines (second-order polynomial fits) in Figure 13.

We see that some of the models with large n (the largest symbols) and small disk masses are very close to the EW = 0 line. Moreover, for late-type Be stars, many of the models with $W1 - W2 \geqslant 0.05$ have a positive Hα EW. Interestingly, for late-type B stars, many objects with a small disk mass (smaller than $10^{-9.5} M_\odot$ for the inclination of $60°$), there is a clear IR excess, indicating the presence of a circumstellar disk, but no significant Hα: such objects could easily elude the Be star classification.

4.4. Disk Growth and Dissipation Phases

As suggested by Vieira et al. (2017), disk growth and dissipation phases can be represented with different combinations of the parameters n and ρ_0. During these formation/dissipation phases, the star is expected to describe a loop in the CMD (Dougherty et al. 1994; de Wit et al. 2006; Sigut & Patel 2013).

Figure 14 shows our confirmed Be stars together with models of disk growth and dissipation phases, similar to those presented by Vieira et al. (2017): first the disk forms and grows in size, represented by a decrease in n from 4 to 3.5 for a constant ρ_0, and then subsequently dissipates, represented by a decrease in ρ_0 and decreasing n. For each stellar model, two different values of ρ_0 at the beginning of the disk growth were considered in an attempt to mimic two different disk mass loss rates.

Models represented by gray circles correspond to a logarithm of the mass loss rates (in $M_\odot$ yr^{-1}) of -9.1 for the B1 star, -10.1 for the B3 star, and -11.1 for the B7 star, as in Vieira et al. (2017). Models indicated with black diamonds represent mass loss rates of an order of magnitude larger and are consistent with the mass loss rates predicted by Granada et al. (2013) from stellar angular momentum loss rates for critically rotating B-type stellar models. The models joined with dashed and dotted lines correspond to disk evolutionary tracks through a formation/dissipation phase for three different inclination angles, 18°, 60°, and 84°. The size of the points increases from pole to equatorial viewing angle. For most of the models, once the disk appears, the star very quickly reaches a large color excess and becomes brighter in the $W1$ band.

We see that, for the confirmed early and mid Be stars, both sets of disk evolutionary tracks qualitatively describe the location of the stars having an excess in $WISE$ colors. The observed late Be stars are better described by disks with the larger density presented here. The large number of Be candidates in this spectral type range that have not been confirmed yet (see Figure 6(b)) shows that smaller disks may be frequent but hard to detect, but this conclusion requires further investigation.

We can see in Figure 14 that $W1 - W2 > 0.15$ is predicted for models with combinations of ρ_0 and n that describe disks being continuously fed by the central star. Therefore, we propose that most Be stars with $W1 - W2 > 0.15$ (observed in particular among mid and early Be stars) host developed, stable disks. Most Be stars with $W1 - W2 \leqslant 0.05$ are likely in a diskless phase, and objects with $W1 - W2$ between 0.05 and 0.15 are either stars with small mass loss rates or objects with dissipating disks.

Following this scheme, and as mentioned before, 53.1% of the early Be stars in our sample and 39.4% of the mid Be stars are in a quiescent or diskless phase. Among active stars, 14.3% of all early Be stars and 9.1% of all mid Be stars have a dissipating or small disk, and 32.7% of early Be stars and 51.5% of mid Be stars have a developed disk. For the overall sample of 80 early and mid Be stars, 46.3% are in a diskless phase, 12.5% have a small or dissipating disk, and 41.3% have a developed stable disk. This last value is consistent with the fraction (37%) of Be stars with long-term photometric variability (Labadie-Bartz et al. 2017).

For objects with $W1 - W2 \geqslant 0.15$, our modeling shows that the allowed combinations of ρ and n that correspond to stable, developed disks, lead to a tight relation between the corresponding Hα equivalent width and the mass of the disk when the inclination angle and the spectral type of the star are fixed. Therefore, in the frame of this simple disk modeling, we suggest that, for very stable disks, we could spectroscopically estimate the mass of the disk using the spectral type of the star, an estimate of the viewing inclination (via the morphology of the Hα emission line), and the EW$_{H\alpha}$.

For three Be stars in our sample with $W1 - W2 > 0.15$ and flagged as stable that are likely to host stable developed disks, there is available data of Hα spectroscopy from the BeSS catalog: there is one early Be star BD+60 341 (EW$_{H\alpha} = -35.2$ Å), and two mid Be stars: V* V984 Cas (EW$_{H\alpha} = -24.0$), and EM* GGA 93 (EW$_{H\alpha} = -22.2$). The Bess catalog gathers the information of classical Be stars and Herbig Ae/Be stars, and assembles spectra obtained by professional and amateur astronomers of these stars. For the three objects with available spectra, using the relations shown in Figure 13, we obtained disk masses (log(M_{disk})) of -7.302, -8.025, and -8.064, respectively. The green symbols in Figure 13, indicate the values derived from observations, and in all three cases correspond to the upper limit of disk mass.

5. Conclusions

Open clusters provide a unique laboratory to study stellar populations and, in particular, the Be stars. The five young open clusters studied in this work, NGC 663, NGC 869, NGC 884, NGC 3766, and NGC 4755, have long been known to host numerous Be stars that have been broadly studied in the literature. $WISE$ near-IR photometry allows identification of Be stars and the detection of new Be star candidates which could be confirmed spectroscopically. In these clusters, virtually all mid- and early-type Be stars with $W1 - W2 > 0.05$ are known Be stars, which leads us to conclude that, in this spectral range, almost all of Be stars in these clusters have been identified. Conversely, many late-type Be stars may not yet have been identified as such.

BEDISK/BERAY models with typical disk density structures derived for Be stars correctly describe the global near-IR photometric characteristics of Be stars in our sample.

For small and intermediate inclination angles, we obtain that stars with $W1 - W2 \geqslant 0.15$ have values of $n \leqslant 3.5$ and intermediate values of ρ_0. Models with very large disk density do not lead to colors observed in the Be stars of our sample, and the limits we derive are coincident with the disk density "forbidden region" defined by Vieira et al. (2017). For models with large inclination angles (nearly equator-on), the near-IR excesses are rather small, particularly when the central star is of a late spectral type.

The location of the mid- and early-type Be stars with fully-developed disks in the CMD, $W1 - W2 \geqslant 0.15$, requires mass loss rates in agreement with those of Vieira et al. (2017), obtained for a large sample of observed Be stars, and those of Granada et al. (2013) predicted from the stellar angular momentum loss rates obtained for critically rotating models. We find for these stars, if the spectral type and inclination of the central star is known, the disk mass can be estimated from the tight relation between Hα EW and the mass of the disk.

The location of Be stars in $WISE$ CMD and CC diagrams provides a convenient method to separate them into active (Be stars hosting a developed circumstellar disk with $W1 - W2 \geqslant 0.05$) and quiescent stages (Be stars in a diskless phase

with $W1 - W2 < 0.05$). This can be used as a tool to explore the frequency of these different activity states.

From the analysis of Be stars in five open clusters between 15 and 30 Myr, if we understand our observed sample as a snapshot of the behavior of these objects, we deduce that half of the time, early Be stars are in an active phase, while mid Be stars are in an active phase 60% of the time. In particular, 34% of the time, early Be stars seem to host a large, developed disk with $W1 - W2 > 0.15$. For mid Be stars the fraction grows to 51.5%.

Among early and mid Be stars, 15% and 9% of the objects respectively, have $W1 - W2$ between 0.05 and 0.15, which points toward the finding that the formation of small short-lived disks (perhaps from outbursts) is more common among early-type stars, in agreement with other authors (e.g., Hubert & Floquet 1998; Barnsley & Steele 2013; Labadie-Bartz et al. 2017).

In the late B-type group, there is a considerable number of unconfirmed Be candidates. This is why we consider that the sample of late Be stars is not complete enough to make an analysis like the one performed for early and mid Be stars: a large fraction of objects with small infrared excesses might have disks hard to detect from Hα spectroscopy. Near-IR observations in the H band such as those presented by Chojnowski et al. (2015, 2017), or the K and L bands (Lenorzer et al. 2002; Mennickent et al. 2009; Granada et al. 2010; Sabogal et al. 2017), trace the innermost regions of the circumstellar disk, and are more appropriate to study the disks around these late Be stars.

The *WISE* colors of the sample of active Be stars show that early-type objects have more massive disks than late-type Be stars. Some of the models of late-type Be stars with low mass disks in an active phase ($W1 - W2 > 0.05$) have positive equivalent widths, indicating that many late-type stars hosting a disk might be more difficult to detect spectroscopically. This could explain the large number of late Be candidates in our sample.

Finally, the analysis of near-IR photometry of Be stars in open clusters could be useful to explore whether there is a preferential viewing angle in open stellar clusters (i.e., preferential alignment of the stellar rotation axes), as has already been found in certain clusters (Corsaro et al. 2017). Further analysis of *WISE* photometric observations may prove to be a valuable diagnostics for setting constraints on rotating stellar models. Following this work, we plan to analyze Be stars in open clusters of different ages and metallicities.

ORCID iDs

C. E. Jones https://orcid.org/0000-0001-9900-1000
T. A. A. Sigut https://orcid.org/0000-0002-0803-8615
C. Georgy https://orcid.org/0000-0003-2362-4089
S. Ekström https://orcid.org/0000-0002-2564-5660

References

Abad, C., & Garcia, L. 1995, RMxAA, 31, 15
Ahmed, A., & Sigut, T. A. A. 2012, ApJ, 744, 191
Aidelman, Y., Cidale, L. S., Zorec, J., & Arias, M. L. 2012, A&A, 544, A64
Arcos, C., Jones, C. E., Sigut, T. A. A., Kanaan, S., & Curé, M. 2017, ApJ, 842, 48
Balona, L. A., & Koen, C. 1994, MNRAS, 267, 1071
Barnsley, R. M., & Steele, I. A. 2013, A&A, 556, A81
Bonanos, A. Z., Lennon, D. J., Köhlinger, F., et al. 2010, AJ, 140, 416
Bonatto, C., Bica, E., Ortolani, S., & Barbuy, B. 2006, A&A, 453, 121
Chojnowski, S. D., Whelan, D. G., Wisniewski, J. P., et al. 2015, AJ, 149, 7
Chojnowski, S. D., Wisniewski, J. P., Whelan, D. G., et al. 2017, AJ, 153, 174
Cohen, M., Wheaton, W. A., & Megeath, S. T. 2003, AJ, 126, 1090
Corsaro, E., Lee, Y.-N., García, R. A., et al. 2017, NatAs, 1, 0064
Cox, A. N. 2000, Allen's Astrophysical Quantities (4th edn.; New York: AIP Press)
Coyne, G. V., Wisniewski, W., & Otten, L. B. 1978, Publications of the Vatican Observatory, Vol. 1 (Laziale: Vatican Observatory), 257
Cutri, R. M., Wright, E. L., Conrow, T., et al. 2013, yCat, 2328, 0
Davenport, J. R. A., Ivezić, Ž, Becker, A. C., et al. 2014, MNRAS, 440, 3430
de Wit, W. J., Lamers, H. J. G. L. M., Marquette, J. B., & Beaulieu, J. P. 2006, A&A, 456, 1027
Dougherty, S. M., Waters, L. B. F. M., Burki, G., et al. 1994, A&A, 290, 609
Dufton, P. L., Langer, N., Dunstall, P. R., et al. 2013, A&A, 550, A109
Evans, C. J., Smartt, S. J., Lee, J.-K., et al. 2005, A&A, 437, 467
Fabregat, J., & Capilla, G. 2005, MNRAS, 358, 66
Georgy, C., Granada, A., Ekström, S., et al. 2014, A&A, 566, A21
Granada, A., Arias, M. L., & Cidale, L. S. 2010, AJ, 139, 1983
Granada, A., Ekström, S., Georgy, C., et al. 2013, A&A, 553, A25
Grebel, E. K. 1997, A&A, 317, 448
Grebel, E. K., Richtler, T., & de Boer, K. S. 1992, A&A, 254, L5
Gushee, V. M. 1919, AJ, 32, 117
Hoffman, D. I., Cutri, R. M., Masci, F. J., et al. 2012, AJ, 143, 118
Høg, E., Fabricius, C., Makarov, V. V., et al. 2000, A&A, 355, L27
Huang, W., & Gies, D. R. 2006, ApJ, 648, 580
Huang, W., Gies, D. R., & McSwain, M. V. 2010, ApJ, 722, 605
Hubert, A. M., & Floquet, M. 1998, A&A, 335, 565
Hunter, I., Brott, I., Langer, N., et al. 2009, A&A, 496, 841
Iqbal, S., & Keller, S. C. 2013, MNRAS, 435, 3103
Ita, Y., Matsuura, M., Ishihara, D., et al. 2010, A&A, 514, A2
Jarrett, T. H., Cohen, M., Masci, F., et al. 2011, ApJ, 735, 112
Jaschek, M., & Egret, D. 1982, in IAU Symp. 98, Be Stars, ed. M. Jaschek & H.-G. Groth (Cambridge: Cambridge Univ. Press), 261
Jones, C. E., Molak, A., Sigut, T. A. A., et al. 2009, MNRAS, 392, 383
Jones, C. E., Tycner, C., Sigut, T. A. A., Benson, J. A., & Hutter, D. J. 2008, ApJ, 687, 598
Keller, S. C., Grebel, E. K., Miller, G. J., & Yoss, K. M. 2001, AJ, 122, 248
Kharchenko, N. V., Piskunov, A. E., Roeser, S., Schilbach, E., & Scholz, R.-D. 2013, yCat, 355, 80053
Koenig, X. P., Leisawitz, D. T., Benford, D. J., et al. 2012, ApJ, 744, 130
Kohoutek, L., & Wehmeyer, R. 1997, AAHam, 11, 1
Labadie-Bartz, J., Pepper, J., McSwain, M. V., et al. 2017, AJ, 153, 252
Lavdovsky, V. V. 1961, TrPul, 73, 5
Lenorzer, A., de Koter, A., & Waters, L. B. F. M. 2002, A&A, 386, L5
Maciejewski, G., & Niedzielski, A. 2007, A&A, 467, 1065
Maeder, A., Grebel, E. K., & Mermilliod, J.-C. 1999, A&A, 346, 459
Marco, A., & Bernabeu, G. 2001, A&A, 372, 477
Marsh Boyer, A. N., McSwain, M. V., Aragona, C., & Ou-Yang, B. 2012, AJ, 144, 158
Martayan, C., Baade, D., & Fabregat, J. 2010, A&A, 509, 11

Mathew, B., & Subramaniam, A. 2011, BASI, 39, 517
McSwain, M. V., & Gies, D. R. 2005, ApJS, 161, 118
McSwain, M. V., Huang, W., & Gies, D. R. 2009, ApJ, 700, 1216
Mennickent, R. E., Sabogal, B., Granada, A., & Cidale, L. 2009, PASP, 121, 125
Moffat, A. F. J., & Vogt, N. 1974, VeBoc, 2, 1
Moitinho, A., Alfaro, E. J., Yun, J. L., & Phelps, R. L. 1997, AJ, 113, 1359
Nikutta, R., Hunt-Walker, N., Nenkova, M., Ivezić, Ž., & Elitzur, M. 2014, MNRAS, 442, 3361
Okazaki, A. T., Bate, M. R., Ogilvie, G. I., & Pringle, J. E. 2002, MNRAS, 337, 967
Oktariani, F., Okazaki, A. T., Kunjaya, C., & Aprilia 2016, MNRAS, 459, 4440
Oudmaijer, R. D., & Parr, A. M. 2010, MNRAS, 405, 2439
Phelps, R. L., & Janes, K. A. 1994, ApJS, 90, 31
Piatti, A. E., Clariá, J. J., & Bica, E. 1998, ApJS, 116, 263
Pigulski, A., Kopacki, G., & Kołaczkowski, Z. 2001, A&A, 376, 144
Rivinius, T., Carciofi, A. C., & Martayan, C. 2013, A&ARv, 21, 69
Sabogal, B. E., Ubaque, K. Y., García-Varela, A., Álvarez, M., & Salas, L. 2017, PASP, 129, 014203
Sana, H., de Mink, S. E., de Koter, A., et al. 2012, Sci, 337, 444
Sanner, J., Brunzendorf, J., Will, J.-M., & Geffert, M. 2001, A&A, 369, 511

Sigut, T. A. A. 2011, in IAU Symp. 272, Active OB stars: structure, evolution, mass loss, and critical limits, ed. C. Neiner et al. (Cambridge: Cambridge Univ. Press), 426
Sigut, T. A. A., & Jones, C. E. 2007, ApJ, 668, 481
Sigut, T. A. A., McGill, M. A., & Jones, C. E. 2009, ApJ, 699, 1973
Sigut, T. A. A., & Patel, P. 2013, ApJ, 765, 41
Sigut, T. A. A., Tycner, C., Jansen, B., & Zavala, R. T. 2015, ApJ, 814, 159
Silaj, J., Jones, C. E., Sigut, T. A. A., & Tycner, C. 2014, ApJ, 795, 82
Silaj, J., Jones, C. E., Tycner, C., Sigut, T. A. A., & Smith, A. D. 2010, ApJS, 187, 228
Slesnick, C. L., Hillenbrand, L. A., & Massey, P. 2002, ApJ, 576, 880
Slettebak, A. 1985, ApJS, 59, 769
Tadross, A. L. 2001, NewA, 6, 293
Tycner, C., Jones, C. E., Sigut, T. A. A., et al. 2008, ApJ, 689, 461
Vieira, R. G., Carciofi, A. C., Bjorkman, J. E., et al. 2017, MNRAS, 464, 3071
Wenger, M., Ochsenbein, F., Egret, D., et al. 2000, A&AS, 143, 9
Wildey, R. L. 1964, ApJS, 8, 439
Worthey, G., & Lee, H.-c. 2011, ApJS, 193, 1
Wray, J. D. 1966, PhD thesis, Northwestern Univ.
Wright, E. L., Eisenhardt, P. R. M., Mainzer, A. K., et al. 2010, AJ, 140, 1868
Yuan, H. B., Liu, X. W., & Xiang, M. S. 2013, MNRAS, 430, 2188